

Uranium-series disequilibria in MORB, revisited: A systematic numerical approach to partial melting of a heterogeneous mantle

Lynne J Elkins¹ and sarah lambart¹

¹Affiliation not available

December 18, 2023

Hosted file

MORB modeling Data Object S2.zip available at <https://authorea.com/users/560997/articles/674283-uranium-series-disequilibria-in-morb-revisited-a-systematic-numerical-approach-to-partial-melting-of-a-heterogeneous-mantle>

Hosted file

MORB modeling Table S2.xlsx available at <https://authorea.com/users/560997/articles/674283-uranium-series-disequilibria-in-morb-revisited-a-systematic-numerical-approach-to-partial-melting-of-a-heterogeneous-mantle>

Hosted file

MORB modeling Table S1.xlsx available at <https://authorea.com/users/560997/articles/674283-uranium-series-disequilibria-in-morb-revisited-a-systematic-numerical-approach-to-partial-melting-of-a-heterogeneous-mantle>

Hosted file

MORB modeling Table 2 2023-10-24.xlsx available at <https://authorea.com/users/560997/articles/674283-uranium-series-disequilibria-in-morb-revisited-a-systematic-numerical-approach-to-partial-melting-of-a-heterogeneous-mantle>

Hosted file

MORB modeling Table 1 2023-10-24.xlsx available at <https://authorea.com/users/560997/articles/674283-uranium-series-disequilibria-in-morb-revisited-a-systematic-numerical-approach-to-partial-melting-of-a-heterogeneous-mantle>

Hosted file

MORB modeling Data Object S1.zip available at <https://authorea.com/users/560997/articles/674283-uranium-series-disequilibria-in-morb-revisited-a-systematic-numerical-approach-to-partial-melting-of-a-heterogeneous-mantle>


Uranium-series disequilibria in MORB, revisited: A systematic numerical approach to partial melting of a heterogeneous mantle


Lynne J. Elkins*¹, Sarah Lambart²

¹ University of Nebraska-Lincoln, Lincoln, NE, USA

5 ² The University of Utah, UT, USA

* elkins@unl.edu [corresponding author]

 ORCID (FA): 0000-0002-0903-7091

 ORCID (SA): 0000-0002-3636-7950

Keywords: Mid-ocean ridge basalt; pyroxenite; modeling; U-series

10 **Abstract**

Here we present systematic, computational modeling outcomes for bilithologic mantle melting in divergent mid-ocean ridge environments. We present outcomes for equilibrium and disequilibrium porous flow melting for mantle containing 0-50% pyroxenite in thermal equilibrium with fertile peridotite, for potential temperatures of 1300 and 1400°C, solid upwelling rates from 1-50 cm/yr., and residual maximum porosities of 0.1-2.0%. Our calculations support a multi-lithologic, globally heterogeneous mantle that also melts in a heterogeneous manner. Melting of peridotite alone can reproduce some but not all global MORB data. Silica-excess pyroxenites can uniquely produce low ($^{226}\text{Ra}/^{230}\text{Th}$) and ($^{231}\text{Pa}/^{235}\text{U}$) with high ($^{230}\text{Th}/^{238}\text{U}$), but quantities greater than ~10% also produce anomalously thick crust, restricting their likely abundance. Silica-deficient pyroxenites produce more moderate outcomes, except for chemical disequilibrium transport scenarios with unrealistically high ($^{231}\text{Pa}/^{235}\text{U}$). We also show that U-series disequilibria in partial melts can be decoupled from trace element compositions by radioactive decay during transport in two-dimensional regimes.

1 Introduction

Partial melting of the convecting and decompressing mantle is the dominant mechanism of magma production on Earth, and is responsible for generating the majority of the planet's volcanic activity. Our understanding of the mantle melting process, which drives the formation of oceanic crust, is nonetheless incomplete, and a number of fundamental questions remain unresolved. One is the role that multiple lithologies residing in the decompressing mantle might have in generating partial melts and, thus, oceanic crust (e.g., Hirschmann and Stolper 1996). Although volumetrically minor compared to the dominant ultramafic rocks, recycled and reworked mafic lithologies may play an outsized role in generating oceanic magmas due to their distinct melting behavior (e.g.,

Hirschmann and Stolper 1996; Kogiso et al. 2004; Lambart et al. 2013; Stracke and Bourdon 2009; Stracke et al. 2006). One reason for that incomplete understanding is that geochemical indicators of mantle melting, as recorded in basaltic lavas extracted from that mantle, are relatively ambiguous regarding the lithologic types involved in the partial melting process (e.g., Hirschmann and Stolper 1996; Lang and Lambart 2022; Mallik et al. 2021; Stracke and Bourdon 2009). Partial melting is a prolonged and progressive process that occurs over a significant depth range (e.g., Asimow et al. 1995), and the magmas thus produced are mixed and homogenized to an unknown degree prior to emplacement, processes which obscure subtle lithologic melting signals (e.g., Stracke and Bourdon 2009). Thus, although the trace element and radiogenic isotope compositions of mid-ocean ridge basalt (MORB) lavas indicate the mantle is chemically heterogeneous over long time- and length scales (e.g., Hirschmann and Stolper 1996; Kogiso et al. 2004; Rudge et al. 2013), the lithologic characteristics of those heterogeneities is less clearly constrained.

Uranium-series isotopic disequilibria record different information about the mantle melting regime than traditional chemical concentration and radiogenic isotopic data. The U-series decay chains are sensitive not only to trace element abundances and partitioning in the presence of residual minerals, but also to the timescales of melting and melt-rock chemical interactions during magma transport (e.g., McKenzie 1985; Williams and Gill 1989). The system is notably sensitive to melting rates, in addition to the expected controls on trace element partitioning (i.e., the source rock's residual mineralogy during melting) (e.g., Williams and Gill 1989). In fact, U-series disequilibria remain the only geochemical measurements that directly record timing information about mantle melting, making the data a useful complement to traditional major element, trace element, and radiogenic isotope geochemistry.

Mafic rocks like pyroxenites melt at overall faster rates and with different residual mineralogy than ultramafic peridotites, and are thus predicted to generate lavas with detectable geochemical signatures (e.g., Hirschmann and Stolper 1996; Pertermann et al. 2004; Stracke et al. 2006; Yang et al. 2019). During decompression along a given mantle adiabat, a pyroxenite source rock should thus produce partial melts with compositions that are different from peridotitic melts, and past work suggests this difference is detectable for U-series disequilibria (e.g., Elkins et al. 2019; Koornneef et al. 2012; Prytulak and Elliott 2009; Russo et al. 2009; Stracke et al. 2006). However, due to the complexity of the system, the U-series approach requires the comparison of measured data with complex, time-dependent, progressive melting models, and interpretation of measured results can be muddled by difficulties interpreting non-unique and overlapping model outcomes. Recent work by Elkins et al. (2019, 2023), among others (e.g., Prytulak and Elliott 2009; Stracke et al. 2006; Waters et al. 2011), suggests that it is nonetheless possible to

place constraints on the mantle melting process of a heterogeneous mantle. For instance, the authors showed that the range of U-series isotope disequilibria observed in global oceanic basalts, particularly when only plausible scenarios for mid-ocean ridge and ocean island melting environments are considered (e.g., faster upwelling at most hotspots than beneath passively upwelling divergent regions), supports the involvement of pyroxenite in the partial melting of the sub-oceanic mantle (Elkins et al. 2019, 2023). New model developments by Elkins and Spiegelman (2021) have provided a set of expanded tools that additionally incorporate chemical equilibration rates in steady-state melting calculations.

To more thoroughly investigate the role of heterogeneous melting in magma generation in mid-ocean ridge settings, here we present the results of a systematic study of bi-lithologic (peridotite + pyroxenite) melting in adiabatically decompressing mantle regimes. We have conducted this work using a range of porous flow models, from full chemical equilibration during melting and melt transport (i.e., equilibrium porous flow, after Spiegelman and Elliot (1993) and Spiegelman (2000)) to complete disequilibrium transport (using the new methods of Elkins and Spiegelman (2021)). To capture much of the different pyroxenite melting behavior that is possible in the mantle, we also considered four distinct pyroxenitic lithologies, each coexisting with fertile peridotite in abundances ranging from 1% to 50% of the solid mantle source, and for mantle potential temperatures of 1300°C and 1400°C. For each scenario, we also computed outcomes over a range of solid mantle upwelling rates and maximum residual melt porosities in a compacting medium, after Spiegelman and Elliott (1993), Spiegelman (2000), and Elkins and Spiegelman (2021). As explored further below, we additionally tracked a number of other variables in selected test cases, including aging of the extracted, pooled magma during lithospheric ascent, the effects of heterogeneous melting on trace element ratios, and the effects of integration over a triangular melting regime with different magma transport rates. Altogether, we synthesize the outcomes of approximately 10,000 model calculations, and use them to assess the sensitivity of U-series disequilibria to a series of factors (i.e., mantle temperature, pyroxenite type, pyroxenite abundance, magma transport mechanisms, aging during transport, and two-dimensional melt pooling) in the melting process beneath the global mid-ocean ridge system.

2 Background

Olivine-poor, pyroxene-rich mafic lithologies, hereafter called “pyroxenites” (after, e.g., Hirschmann and Stolper, 1996), constitute a minor (likely ~2-5% on average) but important lithology in the upper mantle, and span a broad range of compositions and thus disparate melting behaviors (e.g., Kogiso et al. 2004; Lambart et al. 2013) that

likely reflect diverse lithological origins (e.g., Downes 2007). While most pyroxenites have lower solidus temperatures and more compressed melting intervals than peridotites, suggesting they could contribute an outsized portion to mixed mantle melts, other types more closely overlap peridotites in melting behavior (Lambart et al. 95 2016). The melting characteristics of a multi-lithologic, heterogeneous mantle source introduces additional complexity, as coexisting lithologies can exchange heat and thereby affect the melting behavior and productivity of their neighbors, in a manner that depends on the proportions and energy budgets of each rock type (e.g., Lambart et al. 2016; Stolper and Asimow 2007).

100 The global geochemical data set for MORBs includes a large number of major element, trace element, and long-lived radiogenic isotope compositions, as well as a smaller (but globally-spanning) U-series disequilibrium data set (e.g., Elkins et al. 2019; Gale et al. 2013, 2014) (Figure 1). Among these and other oceanic basalt data, a variety of major element and trace element characteristics have been proposed as possible indicators of pyroxenite melting in the mantle, including low SiO₂ coupled with high FeO (Lambart et al. 2009, 2013), high TiO₂ contents (Prytulak 105 and Elliott, 2007), and a variety of elemental ratios (e.g., Mn/Fe, Zn/Fe, Ge/Si, Ba/Th, La/Nb, Sr/Nd, Ba/Ta, Nb/Zr) (e.g., Lang and Lambart 2022; Le Roux et al. 2010; Stracke and Bourdon 2009; Yang et al. 2019, 2020). Likewise, although radiogenic isotope compositions may record more complex origins that could become decoupled from source lithology, it is expected that many pyroxenites have time-integrated isotope signatures that record incompatible element enrichment over long timescales, i.e., high ⁸⁷Sr/⁸⁶Sr, ²⁰⁶Pb/²⁰⁴Pb, ²⁰⁷Pb/²⁰⁴Pb, and ²⁰⁸Pb/²⁰⁴Pb, 110 and low ¹⁴³Nd/¹⁴⁴Nd and ¹⁷⁶Hf/¹⁷⁷Hf, due to their posited recycled origins (e.g., Blichert-Toft et al. 1999; Millet et al. 2008; Salters and Dick 2002; Schiano et al. 1997; Sobolev et al. 2008). More recently, there has been a growing interest in non-traditional stable isotopes for further deciphering the origins of erupted basalts. However, increasing analytical precision and a deeper understanding of isotopic fractionation between mantle minerals and melts are needed to effectively use these novel isotopes (e.g., Soderman et al. 2022, and references therein).

115

Uranium-series isotopes record trace element fractionations between decay chain nuclides that occur over timescales similar to the half-lives of those nuclides. In a partial melting process, prolonged residence times in the two-phase (liquid and solid) system can enhance nuclide fractionations due to linked decay effects within the decay chain (e.g., Bourdon et al. 2003; Williams and Gill 1989). The U-series isotope system is thus especially sensitive 120 1) to trace element fractionations (controlled by melt fractions and residual mineralogy) and 2) to the interaction times between the decompressing solid matrix and the migrating magmatic fluid (controlled, in turn, by the solid mantle upwelling rate, the melting rate or productivity of the rock itself, and the porosity and permeability of the

system, which influence magma ascent rates). As pyroxenite rocks have distinct mineralogy, melting depths, and melt productivity characteristics from peridotites, the disequilibria generated between U-series nuclides by pyroxenite melting is likewise expected to be distinct (e.g., Koornneef et al. 2012; Prytulak and Elliott 2009; Russo et al. 2009; Stracke et al. 2006).

In particular, U is less incompatible than Th in garnet, producing ($^{230}\text{Th}/^{238}\text{U}$) activity ratios greater than 1 in partial melts (Beattie 1993; La Tourette et al. 1993). Clinopyroxene, on the other hand, has a partitioning ratio $D_{U}^{\text{mineral/melt}}/D_{\text{Th}}^{\text{mineral/melt}}$ closer to unity; though at moderately low mantle pressures where clinopyroxene is relatively poor in aluminum, Th is somewhat less incompatible than U, potentially generating ($^{230}\text{Th}/^{238}\text{U}$) ≤ 1 in shallow partial melts (e.g., Blundy and Wood 2003, and references therein). Most MORB that are unaffected by post-eruptive decay or by low-temperature chemical weathering reactions (i.e., young, unaltered lavas) have measured ($^{230}\text{Th}/^{238}\text{U}$) > 1 (see data compilations from, e.g., Elkins et al. 2019; Lundstrom 2003; Stracke et al. 2006; and references therein), suggesting melting initiates in the garnet stability field, which in turn suggests depth and temperature limits on upper mantle conditions for a peridotite source. For pyroxenite rocks, however, garnet is stable over a broader depth range and to shallower depths than in peridotites (Kogiso et al. 2004). Hence, if mantle melting is multilithologic and incorporates garnet-bearing mafic source rocks, evidence for residual garnet in the melting zone does not clearly constrain the melting depth (or, by extension, the local mantle temperature) (e.g., Hirschmann and Stolper 1996).

Prior modeling efforts that have attempted to better predict peridotite and pyroxenite melting effects on basalt U-series compositions have largely focused on steady-state, one-dimensional solutions to two-phase (liquid and solid) transport and radioactive decay, and have employed a combination of techniques: 1) reactive porous flow models that track progressive melting over time, while assuming full chemical equilibrium between solid and liquid at all depths (after Spiegelman and Elliott 1993), and 2) classic dynamic melting after McKenzie (1985) and Richardson and McKenzie (1994), with a fixed critical melt porosity threshold and pure disequilibrium chemical transport for melt fractions beyond that threshold. These two models have long represented conceptual “end member” approaches to progressive melt tracking, where porous flow has largely been used to address progressive chemical equilibrium melting with accompanying chromatographic effects, and dynamic melting simulates a near-fractional scenario. There are, however, other differences between the two approaches; for instance, while both models consider radioactive decay of U-series nuclides over time in a progressively decompressing system, porous flow models further consider solid compaction and variable melt porosities with depth. Because near-fractional dynamic

melting models strip trace elements out of the solid matrix very efficiently, calculated aggregated melt compositions
155 tend to be dominated by those fractions generated in the deep melting regime; but preserving short-lived isotopic
disequilibria like ($^{226}\text{Ra}/^{230}\text{Th}$) from the deeper mantle to eruption then requires rapid magma transport rates as high
as 50-500 meters per year over much of the melting regime (e.g., Stracke et al. 2006). Efforts to more fully
characterize dynamic melting outcomes by Stracke et al. (2006) have also suggested additional relationships that
may be difficult to explain, such as systematic changes in the solid upwelling rates within a triangular melting
160 regime, or an apparent lack of correlation between residual mantle porosity and associated magma flow rates.

On the other hand, the reactive porous flow calculator of Spiegelman (2000), based on the model of Spiegelman
and Elliot (1993), assumes instantaneous chemical equilibration between the migrating magma and solid matrix,
which is unlikely to always occur, even in some low-porosity regions experiencing slow capillary flow (e.g.,
165 Iwamori 1993; Kelemen et al. 1997; Spiegelman and Kenyon 1992). It is instead likely that the natural melting
environment is more complex, consisting of a range of chemical equilibration conditions and pathways that
incorporate aspects of both classical models (e.g., Jull et al. 2002; Sims et al. 2002; Spiegelman and Kelemen
2003). Nonetheless, none of these modeling approaches to the melting environment have been systematically
explored for U-series disequilibria from a lithologically heterogeneous mantle.

170 Stracke et al. (2006) did conduct systematic dynamic melting tests of mantle melting in oceanic settings using an
incremental melting model that incorporated magma transport time, and their study incorporated one set of results
for pyroxenite + peridotite bilithologic melting for comparison with peridotite calculations. Their results suggested
that certain observed compositions in the global oceanic basalt data set (particularly elevated ($^{231}\text{Pa}/^{235}\text{U}$) and
175 ($^{226}\text{Ra}/^{230}\text{Th}$) with low ($^{230}\text{Th}/^{238}\text{U}$)) are difficult to produce by peridotite melting, and may be better explained by
melting of a mantle containing small quantities of recycled mafic rocks. Their results also suggested that it is
possible to generate partial melts with the opposite sense of U-series disequilibria (that is, low ($^{231}\text{Pa}/^{235}\text{U}$) and
($^{226}\text{Ra}/^{230}\text{Th}$) with high ($^{230}\text{Th}/^{238}\text{U}$)) if residual porosities are high and both solid upwelling and magma transport
are very slow, though we note that 1) such compositions are typically observed in enriched MORB and at hotpots
180 or in mid-ocean ridge environments near hotspots, where upwelling rates are expected to be higher, and 2) it may
be difficult to mechanistically explain why the extracted fluid would migrate slowly despite the presence of high
residual porosities during melting. Stracke and Bourdon (2009) determined mantle trace element abundances using
a series of dynamic melting calculations for a pyroxenite-bearing melt source, and similarly suggested that mafic
lithologies may be involved in partial melting for much of the oceanic basalt data set. Their study was limited to

185 near-fractional transport regimes, assumed that the decompressing and melting peridotite and pyroxenite lithologies remained thermally isolated and did not exchange heat, and considered relatively high mantle potential temperatures of 1400 °C.

In more recent work, Elkins et al. (2019) conducted bilithologic melting calculations for two types of pyroxenite
190 (Gb108, a silica-excess pyroxenite, and MIX1G, a silica-deficient pyroxenite composition), both present as 10% of the solid source mantle with 90% fertile peridotite. Their modeling considered the petrologic modeling results from a series of one-dimensional melting columns, using mineral modes and liquid abundances predicted by the *Melt-PX* (Lambart et al. 2016) and *pMELTS* models (Ghiorso et al. 2002) after the methods of Lambart (2017), for an average mantle potential temperature (T_p) of 1300 °C to simulate mid-ocean ridge environments. Their
195 calculations permitted non-linear changes in both melt productivity and bulk trace element partitioning with depth during adiabatic decompression, and determined the expected ($^{230}\text{Th}/^{238}\text{U}$), ($^{226}\text{Ra}/^{230}\text{Th}$), and ($^{231}\text{Pa}/^{235}\text{U}$) activity ratios in basalts sampled at the base of the oceanic lithosphere. The U-series melt transport models used in that study were selected to capture the expected end member melting processes, namely equilibrium porous flow and classical dynamic melting, using formulations from Spiegelman and Elliot (1993), Spiegelman (2000), and
200 Richardson and McKenzie (1994). Along with corrected dynamic melting outcomes from Elkins et al. (2023), their results suggested that neither dynamic nor equilibrium porous flow melting of a pure peridotitic source rock can fully replicate observed global basalt compositions at mantle potential temperatures of 1300 °C, particularly the elevated ($^{230}\text{Th}/^{238}\text{U}$) ratios observed in many MORB, and including compositions with high ($^{230}\text{Th}/^{238}\text{U}$) and low age-constrained ($^{226}\text{Ra}/^{230}\text{Th}$) and ($^{231}\text{Pa}/^{235}\text{U}$). Again, no single melting scenario from that study can fully replicate
205 the observed MORB ranges at 1300 °C, but their results also suggested that pyroxenite melting may be better able explain some of those geochemical ranges than peridotite alone.

Here we explore bilithologic melting scenarios in greater detail, to address gaps in prior work, with the objective of better constraining the potential impacts of pyroxenite melting on U-series disequilibria in a heterogeneous
210 mantle. With our series of calculations, we hope to more thoroughly explain the possible origins of global oceanic basalts from mid-ocean ridge environments. We also opt for disequilibrium transport models that consider compaction and variable porosity flow, in an effort to simulate fractional and near-fractional melting environments more realistically, and compare those outcomes to more traditional dynamic melting.

215 **3 Modeling Approach**

The degree of chemical disequilibrium between a melt and the solid matrix during decompression melting can be described by a Damköhler number (Da), a unitless ratio between the chemical reaction rate (e.g., the rate of exchange between the migrating solid and its reacting partial melt) and the rate of a physical process, in this case the physical transport rate of the system. Spiegelman and Elliott (1993) assumed an infinite Damköhler number
220 ($Da = \infty$) to model equilibrium porous flow. Here we also present predicted U-series disequilibria in partial melts for porous flow calculations with $Da = 0$ (representing a transport scenario where the coexisting liquid and solid are in pure disequilibrium, i.e. a fractional melt extraction model) and $Da = 0.1$, a near-fractional, intermediate scenario. $Da = 0.1$ corresponds to one-dimensional decompression melting in which physical transport is ten times faster than the chemical equilibration rate, which inhibits the ability of the two-phase (solid and liquid) system to
225 fully reach chemical equilibrium during ascent. This reaction rate-limited approach, after the methods of Elkins and Spiegelman (2021), resembles the mechanistic concept behind dynamic melting (McKenzie 1985), except that the limited chemical interaction between the liquid and solid is controlled by the rate of equilibration itself, rather than by the fixed, critical melt porosity threshold, within which pure chemical equilibrium is locally achieved. That is, because *all* of the liquid is migrating along the same permeable network, there is no fraction that remains trapped
230 in the pore space long enough to fully achieve equilibrium, but also continuously produces an instantaneous extracted melt, as in traditional dynamic melting. In disequilibrium porous flow, the mass fraction of the melt-filled pore space is determined over the full range of melting depths, using a simplified Darcy's Law function with a scaled permeability rate; this porosity fraction influences the differential liquid transport rate relative to the solid in the compacting solid medium (Spiegelman 2000; Spiegelman and Elliott 1993). The modeling approach used
235 here thus may more closely approximate how a decompressing and melting solid is likely to physically and chemically behave (Elkins and Spiegelman 2021; Spiegelman and Elliott 1993), albeit still in a simplified, one-dimensional and steady-state environment.

Aside from the incorporation of lower Damköhler numbers and thus chemical disequilibrium transport, our
240 approach mimics that of Elkins et al. (2019) in calculating the melting behavior and resulting U-series disequilibria in partial melts resulting from adiabatic decompression of coexisting peridotite and pyroxenite in the mantle (see Data Object S1). As shown in Table 1, we consider four types of mantle pyroxenite: G2 (a silica-excess, eclogitic pyroxenite, after Pertermann and Hirschmann (2003a, 2003b)), KG1 (a hybrid composition calculated by mixing peridotite KLB-1 with G2, after Kogiso et al. (Kogiso et al. 1998, 2003)), M7-16 (an iron-rich, silica-deficient

245 pyroxenite that may be a potential source component for MORBs with > 9 wt.% MgO and low Mg# < 67 (where
Mg# = Mg/(Mg+Fe) x 100) (Lambart et al. 2009, 2013)), and MIX1G (a silica-deficient pyroxenite composition
characterized by Hirschmann et al. (2003) and Kogiso et al. (2003) that represents an average mantle pyroxenite
composition). Each melting run assumes an initial subsolidus source that contains between 0% to 50% pyroxenite
in an otherwise peridotitic mantle, in order to capture a wide range of possible scenarios for mantle melting in many
250 settings. Each run also uses a given mantle potential temperature (T_p) of either 1300 °C or 1400 °C, and a final
melting pressure of 5 kbar to represent average oceanic lithospheric thickness. Following Krein et al.'s (2020)
results, we further tested the effect of low potential temperatures ($T_p = 1200$ °C) on melting of a pure peridotitic
mantle (see Section 5.3.3 below). The choice of 5 kbar for the final pressure of melting is based on the average
oceanic lithospheric thickness at oceanic spreading centers, with the assumption that at relatively low pressure, the
255 main magma transport mechanism may be dominated by rapid transport in dikes or porous channels due to
rheological and thermal changes associated with the transition from a convective regime at depth to one dominated
by conductive cooling (e.g., Niu and Hékinian 1997). For selected peridotite runs, we also tested a thinner
lithospheric lid (2-3 kbar; Table 1). These U-series disequilibrium models also require two additional input
parameters: for the one-dimensional, solid mantle upwelling rate (W_0) we considered a range from 0.5 to 50 cm/yr.;
260 and we tested maximum (i.e., “reference”) mass porosity values (ϕ_0) from 0.1 to 2%. The scaled permeability value
of Spiegelman (2000) (k_r) was not considered here, and was fixed at a reference value of 1.0 for all calculations,
which assumes a constant permeability relationship with porosity.

For each run scenario, U-series disequilibrium melting models require stepwise inputs for the degree of melting
265 ($F(z)$) and for the solid/liquid partition coefficients for each of the elements considered ($D_U(z)$, $D_{Th}(z)$, $D_{Ra}(z)$ and
 $D_{Pa}(z)$), each of which is a function of depth (z); these variables are then interpolated over the model domain to
solve for the melt composition. Because mineral/melt partition coefficients for U, Th, Ra, and Pa are not well
characterized for all possible mineral compositions in mantle lithologies, we used fixed mineral/melt partition
coefficients from the most appropriate experimental data available, along with predicted mineral modes from
270 petrologic models to calculate bulk rock D_i values as a function of depth, for all lithologies (see Table 2).

Petrologic constraints on $F(z)$ and on mineral modes with depth were determined using methods after Lambart
(2017) and Elkins et al. (2019) for coexisting peridotite and pyroxenite lithologies. This approach uses the model
Melt-PX (Lambart et al. 2016), a semi-empirical model calibrated using experimentally-determined phase
275 relationships for pyroxenites. We used this model to determine the degree of melting with pressure for coexisting

peridotite and pyroxenite lithologies, while assuming the two rock types exchange heat and are in thermal equilibration but maintain chemical disequilibrium during melting (see Data Object S1). The thermodynamic model *pMELTS* (Ghiorso et al. 2002) can produce unrealistic results when used to determine melt fractions for both peridotites and pyroxenites, but for a given melt fraction and pressure, the model typically predicts the stable residual minerals and modes for each lithology with greater success (e.g., Lambart 2017). Our approach thus uses a combination of empirical experimental constraints and thermodynamic modeling: at a given depth and T_p , *Melt-PX* predicts the percentage of liquid that is generated by each coexisting lithology along an adiabatic decompression path, and *pMELTS* is then used to determine the stable solid mineral assemblage for each lithology at the same pressure and melt fraction. Further details of the computational steps for this method were presented in Lambart (2017), and the mineralogical and melt fraction results of all of our petrologic calculations are provided in Data Object S2 for reference. The predicted mineral modes were then used to generate bulk rock $D_i^{solid/melt}$ partition coefficients as functions of depth (z), and the necessary input data tables were generated for each scenario using the *pyUserCalc* model template (Elkins and Spiegelman 2021).

Based on our results from the approach described above, a series of follow-up tests for select runs were conducted, as explored in further detail below and listed in Table 1. To keep the scope of this study manageable, for these additional analyses we focused only on an average pyroxenite quantity of 10% in the solid source, and intermediate input values of $W_0 = 3$ cm/yr. and $\varphi_0 = 0.8\%$, all for only selected runs (i.e., lithologies and potential temperatures) of particular interest. For these, coexisting selected trace element abundances were determined. We focused on G2, MIX1G, and, for potential temperatures of 1400 °C only, M7-16 pyroxenites. We selected these results for additional testing because the U-series outcomes spanned reasonable ranges that overlapped with global MORBs, and we additionally focused on trace element ratios that have been suggested as possible indicators of pyroxenite melting in the literature (e.g., Lambart 2017; Shorttle et al. 2014; Stracke and Bourdon 2009), particularly Nb/Zr, Ba/Th, and La/Nb. We assumed initial concentrations similar to Salters and Stracke's (2004) DMM estimates for our peridotite source, and used the EM2 composition suggested by Workman et al. (2004) for our pyroxenites, with trace element partitioning as in Table S2. Finally, we also considered the impacts on U-series disequilibria of aging during magma ascent through the lithosphere, and of melt pooling by integration over a triangular melting regime (after, e.g., Asimow et al. 2001; Langmuir et al. 1992) for a range of extracted melt transport rates. Further details of these analyses are explored below.

305

4 Results

4.1 Pure peridotite melting

In our calculations, peridotite melting produces notably low ($^{230}\text{Th}/^{238}\text{U}$) in partial melts at both $T_p = 1300\text{ }^\circ\text{C}$ and $1400\text{ }^\circ\text{C}$, and largely regardless of the melt transport model used or melting conditions (Figure 2 and Data Object S3); follow-up model calculations that tested lower (shallower) final melting pressures (2-3 kbar) to simulate thinner overlying lithosphere did not significantly change these outcomes (Figure 2). A broader range of ($^{226}\text{Ra}/^{230}\text{Th}$) and ($^{231}\text{Pa}/^{235}\text{U}$) can be produced by changing the melting conditions, particularly by lowering the maximum residual porosity; but we observe that varying the solid upwelling rate does not produce significant changes in the calculated activity ratios for peridotite partial melts.

315

The above findings corroborate prior work by Elkins et al. (2019, 2023) using equilibrium porous flow melting, and are similar to their lower temperature ($T_p = 1300^\circ\text{C}$) dynamic melting model outcomes (including the corrected results of Elkins et al. 2023). We note that our more restricted ($^{230}\text{Th}/^{238}\text{U}$) outcomes do differ from some prior outcomes for dynamic melting in the literature (e.g., Stracke et al. 2006). The main differences are: 1) we considered variable melt productivities with depth, with an increasing degree of melting in a given pressure interval as the process continues, similar to predictions of e.g., Asimow et al. (2001), although for dynamic melting the impact of such variations is expected to be limited; and 2) we used the disequilibrium porous flow model after Elkins and Spiegelman (2021) (see Data Object S1), which approaches fractional melting as $Da \rightarrow 0$ but does not assume a trapped liquid fraction, and determines magma migration rates using variable porosities and permeable flow constrained by Darcy's Law.

325

4.1 Bi-lithologic melting outcomes

In our bi-lithologic melting scenarios, the overall impacts of changing reference φ_0 and W_0 values largely match expectations from prior studies (e.g., Bourdon et al. 1996; Elkins et al. 2011, 2016; Lundstrom et al. 1999; Sims et al. 1999; Spiegelman and Elliott 1993; Waters et al. 2011), for both the peridotitic and pyroxenitic aggregated partial melts. The full plotted outcomes for all of our calculations are included in Data Object S3. Broadly, decreasing the reference porosity (φ_0) increases the residence time of the magma in the melt column by decreasing the permeability, and thus the fluid transport velocity; a lower porosity thus generally enhances chemical interactions and isotopic disequilibria in the melt, due to more prolonged ingrowth. Although the influence of

330

porosity on a longer-lived isotope like ^{230}Th is limited, the impact of increased residence time due to slower fluid
335 transport notably enhances the disequilibrium between shorter-lived isotopes (^{231}Pa and, especially, ^{226}Ra) and their
respective radioactive parents. In other words, lower ϕ_0 generally produces higher ($^{226}\text{Ra}/^{230}\text{Th}$) and ($^{231}\text{Pa}/^{235}\text{U}$)
ratios, consistent with the literature.

Decreasing the solid upwelling rate (W_0) likewise increases residence times, but its impact differs from that of
340 lowering the melt-filled reference porosity. When the source rock's residual mineralogy has a relatively large
fractionating effect on the U-series nuclides (e.g., the effect of high garnet mode on U and Th fractionation), slower
upwelling notably enhances ($^{230}\text{Th}/^{238}\text{U}$) activity ratios in partial melts; and in a system where such mineralogy
persists for a greater extent of the melt column, the impact of decreasing W_0 is even greater. In other words, in
345 comparison to peridotite partial melts, partial melts derived from garnet-rich pyroxenites have notably higher
($^{230}\text{Th}/^{238}\text{U}$) ratios with decreasing upwelling rate, because garnet is both more abundant and stable over a larger
range of pressures in this rock type. There is a similar impact on ($^{231}\text{Pa}/^{235}\text{U}$) because of the very incompatible
nature and intermediate half-life of ^{231}Pa , producing positive correlations in model outcomes between ($^{231}\text{Pa}/^{235}\text{U}$)
and ($^{230}\text{Th}/^{238}\text{U}$) in some pyroxenite melting outcomes, while short-lived ^{226}Ra is far less affected by the upwelling
rate.

350 Similar to our outcomes for pure peridotite melting in Figure 2, and even considering the variations due to W_0 and
 ϕ_0 described above, the peridotite partial melts in our bilithologic tests overall exhibit very little variation in
($^{230}\text{Th}/^{238}\text{U}$) and only a limited range of ($^{226}\text{Ra}/^{230}\text{Th}$) and ($^{231}\text{Pa}/^{235}\text{U}$). Outcomes for peridotite-derived melts also
appear quite insensitive to the types and fractions of coexisting pyroxenite in the mantle source. In other words, the
355 effects of thermal exchange between lithologies on the isotopic composition of peridotite melts is limited, even
with a high (50%) fraction of pyroxenite in the source. On the other hand, the type and amount of pyroxenite has a
detectable influence on the resulting *pyroxenite* partial melt compositions, as summarized further below.

The G2 pyroxenite is an eclogitic, relatively high-SiO₂ composition that melts relatively rapidly and with a
360 significantly colder solidus (corresponding to a deeper melt column initiation) than peridotite rocks (Pertermann
and Hirschmann 2003). Its rapid melting rate produces partial melts with relatively low disequilibria for short-lived
nuclides: model results for pyroxenite melting have notably low ($^{226}\text{Ra}/^{230}\text{Th}$) and a wide range of ($^{231}\text{Pa}/^{235}\text{U}$) that
extends to relatively low values (see Data Object S1). In addition, the range of ^{231}Pa behavior produced is heavily
influenced by the melt transport model and the amount of G2 pyroxenite in the source. There is also a wide range

365 of ($^{230}\text{Th}/^{238}\text{U}$) in the melting outcomes, reflecting the dual impacts of garnet stability and modes on model outcomes.

In Figure 3, we further consider the compositions of simple, mass-balanced, binary mixtures of coexisting G2 pyroxenite and fertile peridotite partial melts, for a range of pyroxenite fractions and melt transport scenarios, all while holding W_0 and φ_0 constant at intermediate values of 3 cm/yr. and 0.8 %, respectively. Although this mixing approach is a simple, first-order approach (for instance, there is no guarantee that the transport pathways for pyroxenite and peridotite melts would have the same porosity, or that all of the partial melts would be extracted and mixed with the same efficiency), it is nonetheless illustrative when considering melt mixtures that might occur, and how they could be affected by mass balance weightings. Because pyroxenite and peridotite have strongly contrasting melt productivities over the course of the melting process, the quantity of pyroxenite in the initial solid source exerts a strong control on the compositions of the resulting mixtures. That is, scenarios with 50% pyroxenite result in mixed aggregated melt compositions that are heavily dominated by the pyroxenite melt composition, not only because pyroxenites contain a greater quantity of trace elements, but simply because that lithology contributes an outsize proportion of magma to the binary mixture (that is, systematically greater than the 50% it occupies in the solid, unmelted source). As a result, our calculated magma products span a wide range in ($^{230}\text{Th}/^{238}\text{U}$) when the G2 and peridotite partial melts are mixed, even for such restricted scenarios (Table S1, Figure 3).

Both single-lithology partial melts and the calculated mass-balanced binary mixtures (Figure 4) for a mantle source containing KG1 have notably different U-series disequilibrium characteristics from G2 scenarios. KG1 is a hybrid pyroxenite composition with relatively low SiO_2 content and that more closely mimics the melting behavior and mineral assemblage of a fertile peridotite; there is thus a narrower range of ($^{230}\text{Th}/^{238}\text{U}$) in the predicted KG1 partial melts than we observe in the G2 melts. That said, KG1 generates partial melts with distinct characteristics from peridotite melts, such as particularly high ($^{231}\text{Pa}/^{235}\text{U}$). We note that the ($^{231}\text{Pa}/^{235}\text{U}$) produced by some model runs (particularly chemical disequilibrium transport scenarios) is unrealistic: such high activity ratios are never observed in natural oceanic basalts (Figure 1). While the ($^{226}\text{Ra}/^{230}\text{Th}$) ratios in our KG1 partial melts are lower and more plausibly within the range of observed MORB, they lack some of the corresponding ($^{230}\text{Th}/^{238}\text{U}$) ratios observed in both natural MORB and our calculated G2 melts (see Data Object S3).

The pyroxenite M7-16 represents a comparatively Fe-rich, Si-poor composition, with comparably higher melt fertility and a steeper solidus curve than KG1. The outcomes of melting scenarios with M7-16 thus appear to share

some characteristics with both G2 and KG1 results (Figure 5). ($^{226}\text{Ra}/^{230}\text{Th}$) in M7-16 partial melts is relatively low and spans a limited range that strongly depends on the melt transport model and pyroxenite fraction; but compared to KG1, M7-16 partial melts also exhibit a somewhat wider range of ($^{230}\text{Th}/^{238}\text{U}$), better approaching some observed MORB compositions. As in previous scenarios, the weighted melt mixtures in Figure 5 are again heavily dependent on initial pyroxenite abundance in the source, and this weighting effect limits the range of ($^{230}\text{Th}/^{238}\text{U}$) in our predicted melt mixtures; however, the calculated outcomes do overlap with observed MORB, suggesting they are reasonable outcomes. Finally, the choice of melt transport regime produces significantly different outcomes for this lithology: while M7-16 partial melts produced by chemical disequilibrium transport scenarios exhibit a very wide range of ($^{231}\text{Pa}/^{235}\text{U}$) that spans to unrealistically high values, the equilibrium porous flow melts are less extreme. In summary, despite the fact that M7-16 melting scenarios are unable to explain the lowest ($^{231}\text{Pa}/^{238}\text{U}$) ratios observed in MORB, and some tested outcomes do not agree with observed values, many of the results can plausibly reproduce portions of the natural ranges in measured oceanic basalts.

The final lithology we considered is MIX1G, a silica-deficient garnet pyroxenite with a solidus curve similar to the KG1 solidus, but a higher melt productivity and a mineral assemblage more similar to M7-16. Results obtained with MIX1G are similar to those for M7-16, with a moderate range in ($^{230}\text{Th}/^{238}\text{U}$) in binary melt mixtures that strongly depend on the pyroxenite abundance; a limited range of ($^{226}\text{Ra}/^{230}\text{Th}$) that includes some plausibly low values; and a wide range of ($^{231}\text{Pa}/^{235}\text{U}$), with equilibrium transport results producing a much better fit with the observed MORB compositions than disequilibrium transport.

415

5 Discussion

5.1 Sensitivity of magma compositions to melting variables

Although even this large number of model calculations cannot span all possible melting scenarios for the upper mantle, our systematic tests do reveal some constraints on the circumstances of mantle melting beneath mid-ocean ridge settings. For one, we can identify circumstances which are unable to reproduce observed MORB compositions at all, and thereby limit the range of plausible scenarios. We can then further evaluate the most important factors influencing melt compositions.

420

5.1.1 Pyroxenite type

Here, we first discuss the effects of pyroxenite source composition on melts derived from coexisting peridotites
425 and pyroxenites. We then address the effects of binary mixing between the partial melts of those lithologies, in the
context of the pyroxenite composition. Additional complexities related to magma mixing are addressed further in
the next section, which considers variations in pyroxenite quantity.

The type and composition of pyroxenite present in the melting regime exert a major control over the U-series
430 disequilibrium compositions of partial melts derived from that regime, due to significant variations in residual
mineralogy, melting rates, and melting temperatures among pyroxenite rocks. Many of those variations in melting
behavior were explored by Lambart et al. (2016, 2013). Broadly, more silica-rich, eclogitic pyroxenites (such as
G2) have deeper solidi and melt faster along an adiabatic path than either peridotites or silica-deficient pyroxenites
(like MIX1G), making them more productive and thus generating more magma during decompression melting.
435 Silica-excess pyroxenites also host stable garnet for much of the melting regime, and may contain other, less well-
constrained minerals for U-series behavior during melting, such as quartz (or one of its polymorphs), kyanite, or
feldspars. In contrast, silica-deficient pyroxenites have melting behavior and residual mineralogy that more closely
resembles peridotites (e.g., stable olivine in the partial melting residue).

440 In the presence of ambient peridotite, pyroxenite lithologies are also heated above their own adiabat while below
the peridotite solidus, which enhances early melting (e.g., Hirschmann and Stolper, 1996), but those high melting
rates are then suppressed or significantly reduced after peridotite melting initiates, due to the generally shallower
melting slopes of pyroxenites (Lambart 2017; Lambart et al. 2016). The difference between peridotite and
pyroxenite solidus depths, which in our model simulations is in turn controlled by the pyroxenite composition, thus
445 also plays a role in partial melt compositions.

In our melting tests, we do observe significantly different partial melting outcomes not only between peridotites
and pyroxenites, but among the different types of pyroxenite. Some pyroxenite partial melting results, particularly
for silica-excess G2 pyroxenite, span a notably broad range in ($^{230}\text{Th}/^{238}\text{U}$) along with low ($^{226}\text{Ra}/^{230}\text{Th}$) and variable
450 ($^{231}\text{Pa}/^{235}\text{U}$). Results for other pyroxenite types have less pronounced ($^{230}\text{Th}/^{238}\text{U}$) ranges, and some (e.g., pure KG1
and M7-16 melts) exhibit problematically high ($^{226}\text{Ra}/^{230}\text{Th}$) and/or ($^{231}\text{Pa}/^{235}\text{U}$) that do not resemble observed
MORB, particularly for chemical disequilibrium melting. However, many calculated pyroxenite partial melts do

have the moderately high ($^{230}\text{Th}/^{238}\text{U}$) required by many MORB, suggesting that small amounts of pyroxenite may be widely distributed in the mantle and may indeed influence MORB compositions on a global basis, as suggested by, e.g., Stracke et al. (2006) and Elkins et al. (2019). Likewise, our outcomes expand upon the more limited tests in Elkins et al. (2019), but broadly confirm those results, particularly in support of the observation that peridotite melts alone cannot easily reproduce the high ($^{230}\text{Th}/^{238}\text{U}$), low ($^{226}\text{Ra}/^{230}\text{Th}$), and low ($^{231}\text{Pa}/^{235}\text{U}$) observed in some MORB, while pyroxenite partial melts span far broader ranges. The best matches to global MORB ranges were produced by binary mixing of peridotitic melts with partial melts produced by fertile G2, M7-16, and, for certain MORB compositions, MIX1G: all garnet-rich pyroxenite lithologies with high melt productivities. In comparison, KG1, a lithology that has been proposed as a potential mantle source component for MORBs (e.g., Lambart et al. 2019) and Icelandic basalts (e.g., Hole 2018; Lambart 2017; Shorttle and MacLennan 2011), produces overall similar disequilibria to peridotites in ($^{230}\text{Th}/^{238}\text{U}$) (i.e., too low). However, a higher potential temperature, as expected beneath Iceland, may produce larger isotopic disequilibria by melting of KG1. Alternatively, using a Monte Carlo approach, Brown et al. (2020) suggested that the pyroxenite component beneath Iceland is significantly more enriched in the most incompatible elements (e.g., Rb to Ce) than previously assumed, which would potentially support the involvement of a more fertile pyroxenitic lithology than KG1, assuming trace element abundances are coupled with lithologic major element compositions in the Icelandic mantle source.

Altogether, for the temperatures and conditions considered here, no single pyroxenite lithology (or even binary melt mixtures from a single pyroxenite composition) can fully reproduce all possible MORB compositions in the global data set. For instance, our tested scenarios with G2 in the source are only capable of producing the highest ($^{230}\text{Th}/^{238}\text{U}$) and lowest ($^{226}\text{Ra}/^{230}\text{Th}$) observed in MORB, (i.e., the most extreme compositions in the negative ($^{230}\text{Th}/^{238}\text{U}$)-($^{226}\text{Ra}/^{230}\text{Th}$) global data array (e.g., Sims et al. 2002)), many of which were sampled adjacent to oceanic hotspots (Figure 3). However, more moderate MORB compositions are better reproduced by binary mixtures between peridotite partial melts and melts of M7-16 or MIX1G (Figures 5, 6). ($^{231}\text{Pa}/^{235}\text{U}$), meanwhile, is more strongly influenced by the degree of chemical equilibration during magma transport (see Section 5.1.4 below) than by pyroxenite composition alone. Hence, our results support a global working model in which the mantle source of MORB is populated by a range of recycled mafic rock types.

5.1.2 Pyroxenite abundance

Where varying the pyroxenite composition produces a wide variety of U-series outcomes in partial melts, the amount of pyroxenite in the unmelted mantle source has a more subtle impact on melt compositions. As explored

by Lambart et al. (2016), both the composition and the fraction of pyroxenite in the solid, decompressing source can influence the melting P-T paths of coexisting lithologies, due to the exchange of heat between lithologies and changes to their latent heat budgets. Briefly, the onset of peridotite melting causes a reduction in adjacent pyroxenite melt productivity, and that productivity reduction is greatest for 1) pyroxenites with shallow solidus curves in P-T space and 2) the smallest pyroxenite quantities. That is, with a higher proportion of *peridotite*, a greater quantity of latent heat is consumed by the peridotite once it begins melting, which reduces or even stalls simultaneous pyroxenitic melting by scavenging heat from the neighboring pyroxenite rocks. These heat exchange effects can have a notable impact on the respective magma productivity from the two lithologies, without necessarily greatly affecting the total magma production (Lambart 2017; Stolper and Asimow 2007).

Although this complex heat effect can impact the total degrees of melting achieved by coexisting peridotites and pyroxenites, its impact on U-series disequilibria in *peridotite* partial melts appears relatively small (see Data Object S3). In detail, because the mineralogy present in the peridotite residue during progressive partial melting changes little as the coexisting quantity of pyroxenite is changed, the resulting change in U-series disequilibria in the aggregated peridotite melt is also small. The peridotite melt compositions we calculated are thus highly insensitive to the pyroxenite fraction in the source. *Pyroxenite* melt compositions, on the other hand, vary more significantly with the initial pyroxenite fraction (e.g., $^{230}\text{Th}/^{238}\text{U}$) in partial melts increases with greater pyroxenite abundance), though most such changes are still relatively small.

While the impact of pyroxenite quantity on partial melt compositions is relatively small, because the total melt budgets are strongly affected by the quantity of each lithology in the source, the pyroxenite source abundance has a far more pronounced impact on the compositions of mass balanced binary *mixtures* of partial melts from the two coexisting lithologies. That is, if there is more pyroxenite in the solid source, the pyroxenite ultimately contributes a higher proportion of melt to the aggregated mixture, both because the rock type is present in greater quantities and because pyroxenite is more productive overall. The impact of this simple mass balance effect on the compositions of binary melt mixtures can in fact be quite large, causing resulting binary melt mixtures to span wide ranges of U-series disequilibria and trace element compositions (Figures 3-6). While we do not plausibly expect the decompressing upper mantle to contain 50% pyroxenite on a large scale, making our maximum proportion an extreme scenario, we cannot exclude the possibility that locally, high proportions of pyroxenite in the melt zone will melt readily at even moderate potential temperatures, and so may preferentially impact MORB compositions

at such locations. Variations in the pyroxenite quantity in the source could thus help to explain the origins of enriched MORB by melting of increased quantities of pyroxenite.

515 5.1.3 Mantle temperature

We can also identify systematic differences in partial melting outcomes with changes in mantle potential temperature (T_p), and compare our calculated results to measured basalt compositions along with proposed proxies for mantle temperature (e.g., oceanic crustal thickness, which is a product of total overall melting beneath the ridge axis (Bourdon et al. 1996; Klein and Langmuir 1987)). Overall, results for our calculated melt compositions are relatively similar at $T_p = 1300$ and 1400 °C, with overlapping outcomes. However, in a hotter mantle, all lithologies tested here contain stable garnet over an expanded depth range, which permits more prolonged melting in the presence of residual garnet. As a result, higher T_p produces expanded ($^{230}\text{Th}/^{238}\text{U}$) ranges in partial melt compositions for all lithologies. By affecting solidus pressures and thus the depth of the melting regime, higher temperatures also enhance the total quantity and proportion of garnet-bearing pyroxenite partial melts that are contributed to weighted melt mixtures, which likewise produce enhanced ($^{230}\text{Th}/^{238}\text{U}$) in our binary melt mixtures (Figures 3-6). Both of these garnet signature effects (that is, deeper melting overall, and enhanced pyroxenite contributions to melt mixtures) could help to explain the relatively high ($^{230}\text{Th}/^{238}\text{U}$) observed in mid-ocean ridge settings close to hotspots, where both the mantle temperature and the pyroxenite abundance may be relatively high (e.g., Koornneef et al. 2012).

530

Productive melting regimes, whether due to higher potential temperatures or larger quantities of fertile pyroxenites, should generate a high magma flux to the ridge axis and thus produce thickened oceanic crust. Oceanic crustal thickness is inversely related to the seafloor depth, such that axial sampling depth can be used as a rough proxy for thickness (e.g., Klein and Langmuir 1987). We calculated crustal thicknesses and axial depths for weighted mixtures of partial melts from coexisting pyroxenite and peridotite rocks, considering representative model scenarios with average solid mantle upwelling rates of 3 cm/yr. and maximum residual porosity values of 0.8%. We determined crustal thicknesses given the total quantity of melt produced over a 1D melting column for the two melting lithologies, assuming a 15% density contrast between mantle and oceanic crust and full melt extraction to form the crust. We calculated the seafloor depth for a given crustal thickness using a simple isostatic model with 200 km compensation depth, dynamic support of the surrounding plate, and a typical ocean density profile as a reference column, with 7 km crustal thickness, 3 km of ocean water, and underlying layers and densities after Lin et al. (1990). The results of these calculations are shown in Figure 7 and included in Table S1.

540

Overall, increasing the mantle potential temperature of a peridotitic mantle from 1300 to 1400 °C results in limited thickening of the crust. However, for the limited scenarios tested here, a 100 °C temperature range can explain neither the lowest nor the highest axial depths observed at mid-ocean ridges, and, as described in the previous section, produces only a limited range in isotopic disequilibria.

In our models, adding pyroxenite to the source always results in an increase in predicted crustal thickness, though the magnitude of crustal thickening depends highly on the pyroxenite composition and its corresponding melt fertility. Due to its especially high melt productivity and deep solidus, our G2 melting and mixing scenarios span the greatest range of possible outcomes and extend to significant subaerial thickening, particularly at $T_p = 1400$ °C and for eclogite-rich scenarios. While this may suggest that high temperatures and high quantities of silica-excess, eclogitic pyroxenite could help to explain the most thickened oceanic crust, most outcomes involving G2 produce unrealistic crustal thicknesses compared to typical global ridges, so a G2-rich mantle source is a poor fit for most other ridge settings. Considering the high expected density of eclogites and accompanying difficulties in sustaining mantle decompression, we also do not necessarily expect most upwelling mantle to contain extremely high proportions of eclogitic material.

Scenarios for other pyroxenite types tested, such as KG1 and MIX1G, produce partial melt volumes that correspond to much of the observed MORB data set for axial depth, though the selected results shown for these lithologies lack sufficiently high ($^{230}\text{Th}/^{238}\text{U}$) to explain the full data set. Outcomes for the composition M7-16 span a somewhat broader compositional range, but still fail to explain the highest ($^{230}\text{Th}/^{238}\text{U}$) results for regions with thin crust and deep ridge axes. In fact, none of the results shown reproduce the thinnest crust and deepest ridge axes; this is likely because we have limited the scenarios shown to upwelling rates of 3 cm/yr. and 10% pyroxenite in the source; we have thus neglected ultraslow spreading settings where thin crust likely overlies thick, cold mantle lithosphere. Indeed, while the current global data set overall exhibits enough scatter to suggest a lack of simple relationship between crustal thickness and ($^{230}\text{Th}/^{238}\text{U}$), the deepest ridge settings in Figure 7 do correspond to relatively low- ($^{230}\text{Th}/^{238}\text{U}$) basalts from the Gakkel and Southwest Indian Ridges, both ultraslow-spreading centers. A decrease in mantle potential temperature in those settings would decrease the total magmatic productivity and the resulting crustal thickness. Ultraslow divergence rates also permit more conductive cooling at the surface, which is expected to thicken the overlying lithospheric layer and truncate the melting regime at greater depths (Montesi et al. 2011), which would likewise reduce magma production and crustal thickness.

575 Although even more exhaustive modeling calculations of extreme settings (such as ultraslow ridges) were beyond
a reasonable scope for our study, we suspect that a wider range of upwelling rates, residual melt porosities, mantle
temperatures, and lithospheric thicknesses could explain the observed ranges of axial depths and isotopic
compositions in MORBs even more closely. Overall, while our results highlight the fact that large abundances of
highly-fertile eclogite in the mantle source would produce unrealistic crustal thickening for most spreading centers,
580 they are otherwise consistent with a lithologically and thermally heterogeneous mantle source for most MORBs.
Alternative scenarios suggested in the recent literature (e.g., Krein et al. 2020), such as melting of cold, peridotitic
asthenosphere with stable feldspar, are explored further below.

5.1.4 Magma transport regime

5.1.4.1 Two-phase porous flow

585 The model outcomes synthesized above include results from all three of the reactive porous flow magma transport
models tested here, from equilibrium to pure disequilibrium reactive transport, but we observe that the choice of
transport model itself has a major role in partial melting outcomes, particularly for certain pyroxenite compositions.
Debate persists among geochemists regarding the degree of chemical equilibration that likely occurs between
migrating magmas and decompressing host mantle rocks (e.g., Aharonov et al. 1997; Hewitt 2010; Jull et al. 2002;
590 Katz and Weatherley 2012; Kelemen et al. 1997; Kogiso et al. 2004; Sims et al. 2002; Spiegelman et al. 2001;
Spiegelman and Kenyon 1992; Stracke and Bourdon 2009; Weatherley and Katz 2012), and our outcomes shed
additional light on that discussion.

Fluid dynamics and flow models suggest that magma likely migrates through a decompressing rock matrix in a
595 variety of ways, spanning a range of degrees of chemical equilibration (e.g., Spiegelman et al. 2001; Spiegelman
and Kenyon 1992; Weatherley and Katz 2012). Some magma may migrate along small-scale, low-porosity
networks, which permit greater chemical exchange and thus may approach equilibrium porous flow due to slower
flow rates; while other partial melts could experience more rapid (but still restricted), higher-porosity migration
along permeable channels, approaching a “fractional,” chemical disequilibrium style of transport. Likewise, two-
600 porosity models cover a broad, but more poorly constrained range of scenarios than we have examined here, and
have been previously invoked to simulate heterogeneous, two-dimensional flow beneath areas like the East Pacific
Rise (EPR), where young basalts reproduce much of the negative ($^{230}\text{Th}/^{238}\text{U}$)-($^{226}\text{Ra}/^{230}\text{Th}$) array (Figure 1) without

obvious local source heterogeneity, and thus may be better explained by complex flow in a multi-porosity regime than by heterogeneous source effects (Jull et al. 2002; Lundstrom 2000; Sims et al. 2002). While heterogeneous
605 source melting may also contribute to magma production for other data locations included in the negative array (e.g., Stracke et al. 2006; Waters et al. 2011), a range of melt transport regimes likely still exists in the melt zone for global MORB (e.g., Elkins et al. 2019; Katz and Weatherley 2012; Liang 2008; Liang and Parmentier 2010; Weatherley and Katz 2012). The potential impact of transport mechanisms in a heterogeneous mantle on resulting melt compositions thus remains complex and difficult to decipher.

610

Our systematic testing of porous flow models suggests that certain combinations of pyroxenite type and melt transport style simply cannot reproduce observed MORB compositions. For example, a silica-deficient, relatively low fertility pyroxenite (e.g., KG1) that melts fractionally or nearly-fractionally appears to produce magmas with unrealistically high ($^{231}\text{Pa}/^{235}\text{U}$) that have never been observed in natural samples. Outcomes for disequilibrium
615 transport melting of MIX1G and M7-16 are similar, exhibiting excessive ^{231}Pa excesses relative to parent ^{235}U . Equilibrium porous flow melts (and the resulting peridotite-pyroxenite melt mixtures) for all three pyroxenite lithologies, on the other hand, extend to less extreme ($^{231}\text{Pa}/^{235}\text{U}$) while maintaining moderately high ($^{230}\text{Th}/^{238}\text{U}$), more similar to many MORBs (Figures 4-6).

620 While silica-excess G2 overall exhibits some similar melting behavior to the other three pyroxenite lithologies, G2 melting appears distinct in several ways (Figure 3). Partial melts of this lithology, as well as the resulting binary mixtures with partial melts of accompanying peridotite, span a broad range for most calculated activity ratios. Regardless of the melt transport scenario, all G2 partial melts and binary melt mixtures have remarkably low ($^{226}\text{Ra}/^{230}\text{Th}$) along with variable ($^{230}\text{Th}/^{238}\text{U}$), similar to the most geochemically enriched MORB compositions in
625 the global data set. For ($^{231}\text{Pa}/^{235}\text{U}$), while some results are too high to be realistic, some disequilibrium or partial disequilibrium melting outcomes are low enough to overlap the global MORB field, especially at $T_p = 1400$ °C. Similar to other pyroxenite melts, though, the lowest ($^{231}\text{Pa}/^{235}\text{U}$) for a given ($^{230}\text{Th}/^{238}\text{U}$) are outcomes of equilibrium porous flow melting, and only equilibrium scenarios reproduced the most extreme low ($^{231}\text{Pa}/^{235}\text{U}$) and high ($^{230}\text{Th}/^{238}\text{U}$) observed in some MORBs. That said, even neglecting buoyancy arguments, the crustal thickness
630 constraints described above likely limit the abundance of G2-like rocks in the melt regime to under ~10% for typical oceanic settings, especially at high potential temperatures.

Overall, our modeling results suggest that while some disequilibrium melt transport likely plays a global role, low ($^{226}\text{Ra}/^{230}\text{Th}$) and ($^{231}\text{Pa}/^{235}\text{U}$) compositions measured in age-constrained MORBs may require not only the melting of pyroxenite, but also 1) partial melting of small amounts of silica-excess pyroxenites for the most extreme enriched compositions, and particularly, 2) greater degrees of chemical equilibration during melting and magma transport than previously supposed. We suggest this is the case with the necessary caveat that our model does not incorporate the effects of more complex magma mixing and sampling processes that can affect the composition of final aggregated magmas, such as depth-dependent pooling and sampling scenarios proposed by Koornneef et al (2012) and Rudge et al. (2013). While beyond the scope of this study, additional testing of magma pooling and mixing effects would likely be illustrative.

5.1.4.2 Comparison with dynamic melting

Dynamic melting after McKenzie et al. (1985) has previously been invoked to explain mantle melting and the global basalt dataset, most systematically and comprehensively by Stracke et al. (2006), who incorporated magma transport rates after melt extraction as an additional variable in their calculations. Elkins et al. (2019, 2023) also used dynamic melting to simulate high-porosity, channelized flow and efficient melt extraction in a heterogeneous mantle. Here, we used a new dynamic melting python tool developed by Elkins et al. (2023), which incorporates methods from Richardson and McKenzie (1994), Bourdon et al. (2005), and Elkins et al. (2019), and we further incorporated the integration of instantaneous dynamic melts with variable magma extraction rates similar to the incremental computational approach of Stracke et al. (2006). We have used this model to conduct a series of comparison tests between traditional dynamic melting with magma transport and our porous flow models (Data Objects S1, S3). Below, we discuss the main differences between the two models' outcomes.

As described above, the primary computational differences between traditional dynamic melting and our disequilibrium porous flow approach lie in the determination of residual melt porosities and magma transport rates. In the dynamic melting model, melts are extracted either instantaneously (e.g., McKenzie 1985; Richardson and McKenzie 1994; Zou and Zindler 2000) or with a constant, user-defined transport rate (e.g., as in Stracke et al. 2006, and in this study), and always upon reaching a fixed, threshold or critical melt porosity. Melt fractions below the critical porosity threshold are assumed to continuously achieve full chemical equilibrium with the solid matrix, while those that are extracted are fractionally removed and aggregated with no further chemical exchange. Instantaneous melts are thus similar to instantaneous batch melt increments, which are then removed from the system and aggregated. The disequilibrium porous flow model after Spiegelman and Elliott (1993) and Elkins and

Spiegelman (2021), on the other hand, does not utilize a threshold porosity to define magma permeability, flow, or chemical reactivity. Magmas instead continuously react with the solid matrix based on differential transport and reactivity rates; and the magma transport rate itself is controlled by a steadily increasing porosity and permeability function that considers compaction during upwelling and decompression, using Darcy's Law for two-phase flow. Critically, this means that there is no underlying assumption that chemical equilibrium must necessarily be reached, even for a low, melt-filled porosity fraction. The disequilibrium melting formula thus reduces to true fractional melting for stable elements, but incorporates a rate-scaled back-reaction term for partial equilibration with the solid matrix in the case of slower transport.

To more carefully evaluate these model differences, Figure 8 shows a summary of outcomes for dynamic melting of 10% MIX1G and 90% fertile peridotite at 1300 and 1400 °C, using the same solid mantle upwelling rates and threshold porosity values as the solid upwelling rates and maximum or reference porosity values in our porous flow calculations. We additionally tested a range of constant magma transport rates for the extracted, aggregated melt, from extremely slow (1 cm/yr.) to effectively near-instantaneous extraction (1×10^6 cm/yr.) (Data Object S3), similar to the incremental computational approach of Stracke et al. (2006). Figure 8 shows the outcomes for a moderately fast magma transport rate of 10 m/yr., which is similar to the transport rates suggested by Stracke et al. (2006) for MORBs. The calculated dynamic peridotite melt compositions for $T_p = 1300$ °C have very restricted ($^{230}\text{Th}/^{238}\text{U}$), similar to the outcomes for peridotite porous flow melting and the findings of Elkins et al. (2019). Dynamic melting of peridotite at $T_p = 1400$ °C, on the other hand, produces a broader range of outcomes up to ($^{230}\text{Th}/^{238}\text{U}$) ~ 1.2 , as well as a moderate range of ($^{231}\text{Pa}/^{235}\text{U}$), and a positive correlation between those two activity ratios. Similar to prior findings, however, we found that it was not possible to preserve ($^{226}\text{Ra}/^{230}\text{Th}$) in extracted dynamic melts, even with these moderately rapid extraction rates of 10 m/yr.

Dynamic melting of MIX1G pyroxenite also produces moderately different outcomes from our porous flow scenarios. At $T_p = 1300$ °C, dynamic melting calculations more easily achieve elevated ($^{230}\text{Th}/^{238}\text{U}$) and realistically moderate ($^{231}\text{Pa}/^{235}\text{U}$) and ($^{226}\text{Ra}/^{230}\text{Th}$) than disequilibrium porous flow melting, and can also generate the positive ($^{231}\text{Pa}/^{235}\text{U}$) vs. ($^{230}\text{Th}/^{238}\text{U}$) correlation seen in the peridotite partial melts and previously observed by Stracke et al. (2006). In fact, the overall ranges produced by dynamic melting most closely correspond to our equilibrium porous flow outcomes rather than our results for disequilibrium transport (see more detailed outcomes in Data Object S3). Our calculated outcomes for dynamic melting are similar at elevated $T_p = 1400$ °C, but the moderately fast extraction rates of 10 m/yr. shown in Figure 8 again fail to preserve the ^{226}Ra excesses relative to ^{230}Th that are

observed in most MORBs, perhaps because of the deeper onset of melting and correspondingly longer transport
695 distances for magma extraction.

While dynamic melting of peridotite and pyroxenite can for certain circumstances more readily reproduce some characteristics of MORBs, we find that the ability to reproduce the observed data with dynamic melts nonetheless relies heavily on extracted magma transport rates, which must be extremely rapid to preserve $(^{226}\text{Ra}/^{230}\text{Th}) > 1.0$.
700 It appears that in many cases, magma extraction must be essentially independent of the rest of the melting regime and mechanics, particularly its residual porosity, a requirement that may not be reasonable, since magmatic flow rates are related to fluid permeability (e.g., Spiegelman and Kenyon 1992). That is, for dynamic-style melting to be the best mechanism to explain most global MORBs, magma extraction rates must be quite high, have specific values, and importantly, must vary in ways that appear possibly coincidental and unrelated to the physical regime.
705 As an alternative to this bimodal system that experiences either pure chemical equilibration (for a melt fraction that resides semi-permanently within a trapped pore space) or pure chemical disequilibrium (for an extracted fraction), we assert that the model of disequilibrium porous flow model developed by Elkins and Spiegelman (2021) offers a more realistic approach by considering continuous chemical reactivity that scales with physical transport rates. We thus favor our more restricted results for porous flow regimes, and suggest these newer results may place
710 additional limits on the lithologies, potential temperatures, and transport mechanisms present in the mantle asthenosphere.

5.2 Trace element compositions of bilithologic partial melts

Results from our trace element calculations are shown in a series of panels in Figure 9 and Table S1, along with representative MORB data from the East Pacific Rise (EPR), Juan de Fuca-Gorda, and northern Mid-Atlantic Ridge
715 systems (Elkins et al. 2011, 2014, 2016a, 2016b; Scott et al. 2018; Sims et al. 2002). Although data sets that include both U-series disequilibria and trace element compositions are relatively limited, the global data set shown here spans broad ranges in spreading rate, axial depth, and radiogenic isotope compositions observed in global MORB, making it reasonably representative of global systematics.

720 Because of the limited scenarios tested and shown here, we do not fully reproduce all the characteristics of the overall MORB data set. Since highly incompatible element ratios are not strongly affected by progressive melting (Stracke and Bourdon 2009), some settings also likely require different source trace element initial concentrations than we used in our preliminary tests. For instance, the unusually high Ba/Th ratios observed in some MORB from

places like the Knipovich, Mohns, and Juan de Fuca Ridges may be attributed to enriched lithologies similar to those suggested for the source of Icelandic basalts (e.g., Brown et al. 2020). On the other end, some EPR basalts and lavas from 85 °E along the Eastern Volcanic Zone (EVZ) of the Gakkel Ridge have high ($^{226}\text{Ra}/^{230}\text{Th}$) and very depleted incompatible element ratios (i.e., low Nb/Zr and Ba/Th, and La/Nb>1) that are difficult to reconcile with our modeling results in other ways. For both localities, the trace element ratios point toward a depleted (and peridotitic) source. Sims et al. (2002) observed that the broad measured range in ($^{226}\text{Ra}/^{230}\text{Th}$) and ($^{230}\text{Th}/^{238}\text{U}$) in EPR basalts forms a negative array in otherwise homogeneous EPR N-MORB, and suggested sampling of progressive melts from different depths in a two-porosity melting regime can explain the observed data without the involvement of mantle heterogeneity effects. In this scenario, high ($^{226}\text{Ra}/^{230}\text{Th}$) represents melts extracted from relatively shallow depths. Coupled with the observed variations in La/Nb, these EPR basalts may thus record various degrees of depletion of the residual mantle recorded at the top of the melting column. The Gakkel Ridge, on the other hand, represents the global end member in ultraslow spreading ridges, and is expected to overlie anomalously thick oceanic lithosphere for a ridge axis (Montesi and Behn 2007). Elkins et al. (2014) noted that it would be difficult to preserve such high ^{226}Ra excesses relative to ^{230}Th in magmas during transport through thick lithosphere, and suggested melt-rock interactions may also play a greater role for these lavas, a scenario we cannot readily test here.

Aside from the discrepancies described above, our modeling results suggest that the presence of pyroxenite in the source could produce relatively enriched trace element signatures (high Nb/Zr and Ba/Th and low La/Nb ratios) in partial melts. Stracke and Bourdon (2009), who conducted extensive trace element modeling calculations for dynamic melting of a bilithologic mantle, also observed that, at least for relatively high potential temperatures ($T_p = 1400\text{ °C}$), moderately incompatible trace element ratios in oceanic basalts may generally indicate the involvement of mantle pyroxenite in the global mantle melting regime. Some trace element computations have further shown that at low degrees of peridotite melting (i.e., near the peridotite solidus), mixed peridotite-pyroxenite melts can present particularly elevated Ba/Th and Nb/Zr (e.g., Lambart 2017; Stracke and Bourdon 2009).

On the other hand, because pyroxenitic lithologies usually undergo much higher degrees of melting than ambient peridotite, some pyroxenite partial melts may not ultimately be as enriched (and may even be more depleted) in incompatible trace elements than coexisting peridotite partial melts, due to dilution effects at higher melt fractions (e.g., Lambart et al. 2009). Such a dilution effect is notably visible in our outcomes for binary mixing involving G2, where, despite the pyroxenite-derived melt representing 41% of the mixture (see Table S1), the melt mixture

755 itself has a Nb/Zr ratio closer to the pure peridotite melt than the pure pyroxenite melt. In fact, on the whole, our
computed binary melt mixtures are generally unable to produce the full range of observed trace element ratios in
MORB, even though pure pyroxenite melting spans a far greater range.

As above, we attribute much of this mismatch to the more limited scenarios computed within the scope of this
760 study, but it is complex to predict what factors could improve outcomes and thus plausibly explain global MORB
data. While the range of enriched trace element signatures observed could be interpreted to suggest a higher
proportion of pyroxenite in the mantle source than the scenarios shown in Figure 9, and that might compensate for
the dilution effects of high degrees of pyroxenite melting, such a scenario may also produce unrealistic crustal
thicknesses – particularly for G2 melting (Figure 7). It is, however, possible that some of the observed range can
765 be explained by the presence of higher quantities of less fertile (e.g., silica-deficient) pyroxenite with trace element
enrichment.

Alternatively, as suggested above for other MORB, the trace element compositions of pyroxenite components
present in the source may differ from EM2, i.e., by being significantly more enriched in very incompatible elements.
770 However, to approach the highest Nb/Zr ratios in Figure 9A-F, the pyroxenite component would need to be at least
two orders of magnitude more enriched in Nb and Zr than EM2, which is again relatively unlikely. We instead
suggest a combination of factors may be necessary, where some pyroxenite sources are moderately more trace
element enriched than we have assumed and are also more abundant than 10% of the solid source.

775 Finally, the trace element compositions of enriched MORBs could be disproportionately influenced by melts
derived from pyroxenites, either because these melts were preferentially preserved during magma transport by flow
in chemically isolated channels (Lambart et al. 2019; Lambart et al. 2012; Weatherley and Katz 2012), and/or as a
result of isolated fractional crystallization effects that result in a higher degree of crystallization for peridotite melt
than pyroxenite melt (Neave et al. 2019). While possible, such a scenario requires additional melt sampling
780 variations than what we are able to test here, e.g. preferential sampling from certain melt flow paths or depths (e.g.,
Katz and Weatherley 2012; Rudge et al. 2013; Weatherley and Katz 2012).

5.3 Additional factors in MORB generation

To address further questions raised by the analysis above, we have conducted several supplementary calculations using our 10% MIX1G partial melting results as a representative, intermediate test dataset, aiming primarily to
785 observe how sensitive our model outcomes are to additional factors of interest.

5.3.1 Lithospheric transport effects

The results discussed above predict the maximum isotopic disequilibria produced in partial melts at the base of the lithosphere, and do not consider aging or further chemical interactions that may occur before eruption and emplacement. While this type of model assumes steady-state, paired solid and liquid transport, and thus cannot
790 realistically calculate the impacts of melt-rock chemical interactions during lithospheric transport (and indeed, that consideration is complex enough to justify its own, separate study), it is comparably straightforward to consider the impacts of simple aging and isotopic decay after magma separation from the melt regime. For a lithospheric layer that truncates the melting regime at a final melting pressure of 5 kbar, a rapid transport rate of 15 m/yr. corresponds to a total transport time of 1,024 years. As expected, ~1000 years of radioactive decay has little impact
795 on any the U-series nuclides considered here except for ^{226}Ra , with its comparatively short half-life of 1600 years. Figure 6 graphically illustrates the impact of 1,024 years of radioactive decay on ($^{226}\text{Ra}/^{230}\text{Th}$) ratios for a representative MIX1G partial melt composition. From this illustration, we note that while aging during lithospheric transport or storage could potentially help to explain some MORB compositions with relatively high ($^{230}\text{Th}/^{238}\text{U}$) and ($^{231}\text{Pa}/^{235}\text{U}$), but with low, age-constrained ($^{226}\text{Ra}/^{230}\text{Th}$), especially if transport is slower, such compositions
800 are not typical: low, age-constrained ($^{226}\text{Ra}/^{230}\text{Th}$) in ridge lavas is typically accompanied by similarly low ($^{231}\text{Pa}/^{235}\text{U}$) (e.g., Knipovich and Mohns Ridge MORB (Elkins et al. 2014); Figure 1). Low ($^{231}\text{Pa}/^{235}\text{U}$) cannot as readily be explained by short periods of radioactive decay during magma transport or storage, due to the longer half-life of ^{231}Pa . Limited aging prior to eruption (whether during transport or crustal storage) is thus theoretically a plausible explanation for low ($^{226}\text{Ra}/^{230}\text{Th}$) compositions, but it does not fully explain most observed MORB
805 compositions, particularly for definitively young basalts with eruptive age constraints for ($^{226}\text{Ra}/^{230}\text{Th}$) disequilibria.

5.3.2 Triangular melting regimes

Although far more computationally approachable, the melt regime beneath mid-ocean ridges is not likely to truly resemble a one-dimensional melting column; magmas beneath divergent boundaries are instead likely aggregated

810 over an approximately triangular regime due to mantle convection and corner flow, after Langmuir et al. (1992). Although true two-dimensional flow is more complex than the one-dimensional modeling approach used here, we can approximate two-dimensional effects using a simplified “streamline” integration, as explored by Asimow et al. (2001) and others (e.g., McKenzie and Bickle 1988; Richardson and McKenzie 1994). To accomplish this, we have developed an additional python calculation tool that calculates two-dimensional streamline integration for a simple
815 triangular melting regime, using outcomes from the *pyUserCalc* porous flow melting model used here (Elkins and Spiegelman 2021) (see Data Object S1 and Appendix).

Specifically, our two-dimensional calculator integrates porous flow melting along a one-dimensional column, plus a second path segment where the separated magma migrates along the top of the triangle and experiences simple
820 radioactive decay during transport (Figure 10; see Appendix), simulating pooling of melts at the ridge axis. For U-series disequilibria, the magma transport interval after melt segregation can play an important role in melt compositions, because magma parcels that travel for a long time after separation from the melting regime will experience sufficient radioactive decay to detectably reduce their isotopic disequilibria. This effect is particularly pronounced for nuclides with relatively short half-lives (like ^{226}Ra). Our two-dimensional integration model thus
825 tests a range of lithospheric transport rates for magma extracted from each streamline, producing melting outcomes from very slow to essentially instantaneous transport (which latter scenario is most similar to the integration approach of Richardson and McKenzie (1994) for dynamic melts). Our approach most closely resembles the incremental dynamic melting model with transport rates of Stracke et al. (2006), who tested a wide range of magma transport rates as high as 50 to 500 meters per year, but here it is applied to porous flow melting scenarios. The
830 outcomes for representative 10% MIX1G + 90% peridotite melting scenarios are shown in Figure 11.

Figure 11 illustrates that variable magma transport rates from the outer edges of the melting regime to the ridge axis can explain much of the range in ($^{226}\text{Ra}/^{230}\text{Th}$) observed in the global MORB data set (Figure 1). However, if transport rate alone accounts for much of this range, then transport rates must vary tremendously along the global
835 ridge system: high ($^{226}\text{Ra}/^{230}\text{Th}$) requires unrealistically high magma transport rates of 10,000-100,000 cm/yr (100-1,000 m/yr) for pyroxenite melts. Figure 1 illustrates that the range in ($^{226}\text{Ra}/^{230}\text{Th}$) is more restricted within each spreading center, however, suggesting that more modest variations in magma extraction rates could play a role in producing local ranges. Very rapid magma transport in two-dimensional scenarios generally enhances isotopic disequilibrium in the aggregated melt, because the process more effectively samples deep melts extracted from the
840 outer edges of the triangular regime, and such efficient extraction permits those isotopic disequilibria to survive

transport. For ($^{231}\text{Pa}/^{235}\text{U}$), which is less sensitive to decay than ^{226}Ra , more modestly rapid magma transport rates of 100 – 1,000 cm/yr are necessary to preserve the disequilibria in pyroxenite partial melts, while similarly fast rates can enhance disequilibria in peridotite melts.

845 Slow magma transport after separation, on the other hand, causes most integrated melt compositions to approach lower ($^{226}\text{Ra}/^{230}\text{Th}$) and ($^{231}\text{Pa}/^{235}\text{U}$), which for peridotite melting also approaches the one-dimensional case. This effect likely occurs because deep partial melts lose much of their isotopic disequilibrium signatures during transport. That said, these slow-transport, integrated compositions are not actually the same as the one-dimensional results, and for certain scenarios (e.g., ($^{231}\text{Pa}/^{235}\text{U}$) in MIX1G melts) are in fact notably different. Even with slow
850 extracted magma transport rates, deep magma parcels with trace element budgets from the outer corners of the triangular regime do in fact still reach the ridge axis and aggregate. These deep parcels simply approach secular equilibrium for one or more U-series nuclide pairs due to their long travel intervals, more effectively diluting the aggregated isotopic disequilibrium signatures of the pooled melts. That said, the observed compositional differences between one-dimensional melting and a two-dimensional scenario with very slow transport are mostly
855 small for peridotites and for ($^{226}\text{Ra}/^{230}\text{Th}$), suggesting slow transport may decouple some U-series disequilibria from other melt signatures (such as aggregated stable trace elements). This outcome also resembles predictions of prior work (Reagan and Sims 2001; Stracke et al. 2006).

We further note that geodynamic considerations suggest it would be difficult for melts from the outermost corners
860 of a triangular regime to migrate and pool at the ridge axis, such that smaller total masses of magma (and fewer vertical “streamlines”) should be incorporated. This reduced magma quantity may impact both magma compositions and overall budgets (and, thus, crustal thicknesses and axial depths) (e.g., Montesi et al. 2011). Such an effect would likewise systematically reduce absolute predicted crustal thicknesses such as those shown in Figure 7, but not the relative scale of our results (that is, which scenarios produce thicker crust and which are thinner); and
865 inefficient or incomplete pooling may also slightly reduce the influence of very deep melts incorporated into two-dimensional melt aggregates, even if magma transport is rapid. That said, we do not expect the loss of melts from the outermost triangle corners to significantly change our predicted melt compositions.

5.3.3 Effects of residual plagioclase in mantle lithologies

Recent work by Krein et al. (2020) sheds doubt on some assumptions about the nature of mantle melting, instead
870 supporting suppositions that the mantle is, in fact, relatively cold overall, with typical potential temperatures of
29

~1200 °C, and thus MORB melting may not normally initiate in the garnet stability field for peridotitic lithologies. Rather, Krein et al. (2020) suggest that basalt geochemical signatures previously attributed to the presence of residual garnet in their source may instead be more readily explained by progressive melting of shallow, plagioclase-bearing lherzolite rocks.

875

Some of the evidence suggested by Krein et al. (2020) relies on U-series disequilibria in global MORB, and on U-series modeling calculations that reproduce much of that global data set, particularly relatively high measured ($^{230}\text{Th}/^{238}\text{U}$) that were previously attributed to the effects of residual garnet on trace element residence times during the melting process (e.g., Elkins et al. 2011; Prytulak and Elliott 2009; Sims et al. 1999, 2002; Waters et al. 2011).

880 Krein et al. (2020) note that recent, preliminary experimental measurements of U and Th partitioning between melt and anorthite-rich plagioclase suggest a more major role for residual plagioclase in the shallow melting regime (Sun et al. 2017). However, the role of plagioclase in the melt regime of MORB is poorly constrained by melting models overall, and the work of Krein et al. (2020) did not explore all possible scenarios to further test their working model.

885

The suggestion that plagioclase peridotite melting in a relatively cold, upwelling mantle can more successfully reproduce the high ($^{230}\text{Th}/^{238}\text{U}$) observed in MORB than hotter, deeper (garnet-bearing) peridotite melting scenarios deserves further examination. We have thus conducted additional tests to explore whether and how well the plagioclase lherzolite melting scenario works to reproduce U-series disequilibria in global MORB, using a lower
890 mantle potential temperature of 1200°C and the newer Sun et al. (2017) plagioclase/melt partition coefficients. We also considered a range of lithospheric thicknesses, because all but the thinnest oceanic lithosphere may impact the availability of stable peridotitic plagioclase in the decompressing mantle.

The outcomes of our calculations (Figure 2, Data Object S3) suggest that a colder mantle underlying thin
895 lithosphere that preserves plagioclase in the upwelling regime can indeed generate part of the observed MORB data set, similar to the findings of Krein et al. (2020). However, the circumstances under which this occurs appear considerably limited in both mantle temperatures and final melting pressures: because the lithosphere must be thin to permit the presence of residual plagioclase in the source, this lower-temperature scenario must be limited to settings with faster spreading rates and thin lithosphere. However, as the thickness of the lithosphere beneath
900 spreading centers (far from any hotspots) is expected to increase with decreasing mantle temperature (Montesi et al. 2011; Shen and Forsyth 1995), a low T_p scenario with residual peridotitic plagioclase is unlikely to be able to

explain the full global data set shown in Figure 1. Instead, we posit that both the presence of residual garnet, potentially in pyroxenitic lithologies, and warmer melting must in fact be both involved in some settings beneath the global divergent oceanic ridge system.

905 **5.5 Global generation of MORB by partial melting of a multi-lithologic mantle**

Our computational approach suggests that the generation of magma beneath divergent mid-ocean ridge settings cannot be easily explained by a single, one-size-fits-all scenario. While homogeneous, progressive peridotitic melting can produce some observed compositions, other basalts appear to require a decompressing melt source containing one or more mafic lithologies, in addition to peridotitic rocks. Likewise, no single lithologic pairing can
910 produce all observed MORB compositions at $T_p = 1300\text{-}1400$ °C; and neither can plagioclase-bearing peridotites at 1200 °C. The convecting mantle is thus lithologically heterogeneous in a broad sense. That said, there are also limits on the role pyroxenite can play: while high quantities of productive pyroxenite rocks in the solid source can disproportionately impact the compositions of resulting aggregated melt mixtures, producing a wide range of outcomes that spans much of the global MORB data set, observed oceanic crustal thicknesses limit how large those
915 quantities are likely to be, especially for the most fertile, silica-excess eclogitic pyroxenites and the highest mantle temperatures.

The modes of melting of the mantle and of magma transport are also highly heterogeneous, with an apparent greater contribution from melts that are relatively chemically equilibrated with the decompressing matrix than previously
920 suggested. Protactinium activities, in particular, favor a greater degree of equilibrium magma transport, as chemical disequilibrium melting can produce implausibly high ($^{231}\text{Pa}/^{235}\text{U}$) in pyroxenite partial melts, even when pyroxenite melting appears necessary to explain the observed ($^{230}\text{Th}/^{238}\text{U}$) and ($^{226}\text{Ra}/^{230}\text{Th}$) ratios. Additionally, while partial melts generated by decompressing convection beneath mid-ocean ridges are likely pooled across an approximately two-dimensional regime, which should proportionally increase the contributions of deep melts to the aggregated
925 mixture (i.e., increasing ($^{230}\text{Th}/^{238}\text{U}$) in basalts), U-series disequilibria may become decoupled from trace element compositions in melt aggregates by the time intervals required for magma transport to the ridge axis, making two-dimensional effects on U-series disequilibria difficult to detect.

6 Conclusions

930 Decades of persistent efforts in measuring and attempting to interpret the origins of oceanic basalts using U-series disequilibria have raised questions about the usefulness of the method, because the required melting computations are complex and produce overlapping, sometimes non-unique outcomes. We observe, however, that even for a broad range of melt transport models, from full chemical equilibrium to disequilibrium transport, persistent patterns in melting outcomes emerge. The U-series approach remains the only technique available to gather timing
935 information about magmatic processes in the mantle, so we consider that even somewhat indirect interpretations remain valuable.

Systematic testing of U-series disequilibrium outcomes for bilithologic melting scenarios beneath mid-ocean ridge settings suggest that:

- 940 1) The asthenospheric mantle is broadly compositionally heterogeneous in a lithologic sense, containing not only peridotitic rocks, but a range of multiple types of pyroxenite. While homogeneous peridotite melting can produce some MORB compositions, it is unable to fully reproduce the global data set. Eclogitic, silica-rich pyroxenite zones are uniquely able to produce low ($^{226}\text{Ra}/^{230}\text{Th}$), low ($^{231}\text{Pa}/^{235}\text{U}$), high ($^{230}\text{Th}/^{238}\text{U}$) compositions, while hybrid or silica-deficient pyroxenites can produce more moderate outcomes.
- 945 2) Variations in pyroxenite quantity exert the strongest control over the composition of mass-balanced binary mixtures between peridotite and pyroxenite partial melts in bilithologic regimes. High pyroxenite quantities also generate anomalously thick crust, particularly for silica-excess pyroxenites, which restricts their abundance in most settings to under 10%.
- 950 3) While melting of mantle containing silica-deficient and hybrid pyroxenite compositions are the only scenarios that produced moderately high ($^{230}\text{Th}/^{238}\text{U}$) and intermediate ($^{226}\text{Ra}/^{230}\text{Th}$) and ($^{231}\text{Pa}/^{235}\text{U}$), chemical disequilibrium melting of these lithologies generates unrealistically high ($^{231}\text{Pa}/^{235}\text{U}$), suggesting chemical equilibrium melt transport also plays an important role. Overall, our outcomes favor a greater role for chemical equilibration during melting and magma transport than previous work, suggesting a wide range of magma transport rates are necessary to fully explain the global data set. We take this to mean the
955 mantle melting regime is highly heterogeneous not only in composition, but in melt transport mechanisms, encompassing a range of transport rates and chemical equilibration levels. Relatedly, some local variations in melt composition could be produced by two-dimensional melt aggregation with a range of extracted magma transport rates, particularly for ($^{226}\text{Ra}/^{230}\text{Th}$) and ($^{231}\text{Pa}/^{235}\text{U}$).
- 960 4) Uranium-series disequilibria in partial melts can likewise be decoupled from trace element compositions by variations in magma transport rates in two-dimensional flow regimes.

Appendix

Streamline Integration of Uranium-Series Disequilibria in Partial Melts

A simplified two-dimensional integration approach to partial melting, as illustrated in Figure 10, has previously
965 been explored by a number of authors (e.g., Klein and Langmuir 1987; McKenzie and Bickle 1988; Plank and
Langmuir 1992; Plank et al. 1995; Richardson and McKenzie 1994). The approach assumes simple streamlines of
vertical flow in a steady-state melting regime, which are aggregated in two dimensions along the top of the triangle
defined by decompression in convecting cells beneath mid-ocean ridges (Langmuir et al. 1992, and references
therein). Asimow et al. (2001) have summarized prior explorations of this approach in some detail that we will not
970 reproduce here, except to present the McKenzie and Bickle (1988) approach to calculating average concentrations
in partial melts from an integrated triangular regime:

$$\overline{c_i^f} = \frac{\int_0^z c_i^f(z) F(z) dz}{\int_0^z F(z) dz} \quad (1)$$

where $\overline{c_i^f}$ is the average melt concentration of element i over the entire triangular regime, z is the height in the
melting column, $c_i^f(z)$ is the melt concentration at z , and $F(z)$ is the degree of melting at z .

975

The approach of Elkins and Spiegelman (2021) for porous flow melting computes the natural log of the
concentrations of U-series nuclides in the partial melt; this is because for very small values (such as trace element
abundances), the logs of those values are more stable in numerical calculations. Thus, the values computed by the
numerical solution model are:

980

$$U_i^f(z) = \ln(c_i^f(z)/c_i^0) \quad (2)$$

Given results for a one-dimensional melting calculation with depth using the porous flow model, and known initial
concentrations c_i^0 , the concentrations $c_i^f(z)$ for each nuclide can then be determined from $U_i^f(z)$ model results.
Likewise, the original model inputs include values for $F(z)$, the degree of melting at each depth. It should thus be
985 relatively straightforward to compute average nuclide concentrations integrated over the full depth of the melting
regime, using the method in equation (1).

However, the computation is more complex due to the fact that after each partial melt parcel reaches the top of the decompressing triangular regime, it must leave the melting region and travel along the diagonal upper surface by lithospheric transport, until it is aggregated at the center beneath the mid-ocean ridge axis. For stable elements, as considered by Asimow et al. (2001) and references therein, this transport time is inconsequential; not so for U-series disequilibria, which will necessarily experience radioactive decay during transport. It is this effect that can result in a decoupling between trace element concentration and U-series disequilibria. The values to be integrated are thus not simply the outcomes of partial melting along the one-dimensional, decompressing melt column; they must include an additional, second step of simple radioactive decay over a time interval controlled by the length of their travel path and a transport rate. In other words, while a parcel of melt in the center of the melting regime may upwell through the full height assumed by the one-dimensional column model, parcels located toward the sides cease melting at progressively greater depths with distance from the center, and then must travel longer and longer distances before they are aggregated.

1000

Figure 10 thus illustrates that each melting parcel 1) rises and experiences progressive melting over time, generating isotopic disequilibria in both the solid and liquid; then 2) subsequently, the liquid is extracted and migrates along the top surface of the triangle without additional melting, for a specific period of time. In reality, the transport time interval may be controlled by porous or channelized migration rates along the base of or perhaps within the mantle lithosphere. This transport time is poorly constrained, but, if slow, it could significantly decrease U-series disequilibria in melts from the lateral edges of the melting regime, especially for nuclides with short half-lives like ^{226}Ra . In our model, the time interval of decay for a given parcel is determined using an explicitly defined lithospheric transport rate, with a simple geometric rule for determining the path length along the upper surface of the triangle as a function of the corner angle, θ .

1010

Radioactive decay during the second stage of magma transport is determined using standard radioactive decay equations for U-series nuclides, e.g. after Zou (2007):

$$^{238}\text{U} = ^{238}\text{U}_0 e^{-\lambda_{238}t} \quad (3)$$

$$^{230}\text{Th} = ^{230}\text{Th}_0 e^{-\lambda_{230}t} + \frac{\lambda_{238}}{\lambda_{230} - \lambda_{238}} ^{238}\text{U}_0 (e^{-\lambda_{238}t} - e^{-\lambda_{230}t}) \quad (4)$$

1015

$$\begin{aligned}
^{226}\text{Ra} = & ^{226}\text{Ra}_0 e^{-\lambda_{226}t} + \frac{\lambda_{230}}{\lambda_{226} - \lambda_{230}} ^{230}\text{Th}_0 (e^{-\lambda_{230}t} - e^{-\lambda_{226}t}) \\
& + \frac{\lambda_{230}\lambda_{238}}{\lambda_{230} - \lambda_{238}} ^{238}\text{U}_0 \left[\frac{e^{-\lambda_{238}t} - e^{-\lambda_{226}t}}{\lambda_{226} - \lambda_{238}} - \frac{e^{-\lambda_{230}t} - e^{-\lambda_{226}t}}{\lambda_{226} - \lambda_{238}} \right] \quad (5)
\end{aligned}$$

where the values for t are computed at z using the magma extraction path length (based on z and q) and the extracted magma transport rate. The resulting nuclide concentration values are then integrated over depth, after which they can be used to compute activity ratios in the aggregated melt.

1020 The integration calculation described here relies on the basic assumption that all melts can be gathered efficiently to the ridge axis, where they are pooled and aggregated, although the top of the melting column may typically be truncated by the presence of cold lithosphere which terminates melting. Also, melts produced by streamlines in the outermost corners of the melting regime may not be efficiently aggregated, and may instead be ‘lost’ in the surrounding mantle without reaching the center (e.g., Montesi et al. 2011). And finally, decompression of the
1025 asthenosphere is not actually composed of perfect vertical streamlines; this model, as in all triangular streamline integrations of partial melts, necessarily neglects lateral flow.

Author contributions

L.E. and S.L. conceived of this study together through joint discussions, and both conducted the model calculations.
1030 S.L. primarily conducted Melt-PX and pMELTS calculations, and L.E. primarily conducted U-series and follow-up calculations using pyUserCalc. L.E. wrote the first manuscript draft, and both authors co-edited the submitted draft.

Acknowledgements

1035 We are grateful to M. Spiegelman for thoughtful discussions of the value and applications of our 2021 model, and to K. Sims, M. Spiegelman, and P. Kelemen for illuminating conversations about writing new melting models starting all the way back in 2008. Students J. Messer and D. Andersen are acknowledged for running additional modeling calculations that did not ultimately make it into this manuscript, but were valuable tests of concepts. L.J.E. acknowledges funding support from NSF grant EAR-2046932. S.L. acknowledges funding support from
1040 NSF grant EAR-1946346.

Data availability

Supporting data for this study are available in the data supplements provided, and in the public ENKI GitLab code repository (<https://gitlab.com/ENKI-portal/pyUsercalc>). Current versions of the relevant code and the supplementary data directories have also been archived at doi: 10.5281/zenodo.10030658. [Note to reviewers: this Zenodo DOI is claimed but is not yet shared publicly; we will make the directory public after any requested revisions and edits. The Zenodo Git content matches the GitLab repository, which is our main working code directory.]

References

- Aharonov, E., Spiegelman, M., and Kelemen, P. (1997). Three-dimensional flow and reaction in porous media: Implications for the Earth's mantle and sedimentary basins. *Journal of Geophysical Research: Solid Earth*, 102(B7), 14821-14833. doi:10.1029/97JB00996.
- Aigner-Torres, M., Blundy, J. D., Ulmer, P., and Pettke, T. (2007). Laser ablation ICPMS study of trace element partitioning between plagioclase and basaltic melts: an experimental approach. *Contributions to Mineralogy and Petrology*, 153, 647-667.
- Allègre, C. (1968). ^{230}Th dating of volcanic rocks: a comment. *Earth and Planetary Science Letters*, 5, 209-210.
- Asimow, P. D., Hirschmann, M., Ghiorso, M., O'Hara, M., and Stolper, E. (1995). The effect of pressure-induced solid-solid phase transitions on decompression melting of the mantle. *Geochimica et Cosmochimica Acta*, 59(21), 4489-4506.
- Asimow, P. D., Hirschmann, M. M., and Stolper, E. M. (2001). Calculation of peridotite partial melting from thermodynamic models of minerals and melts. IV. Adiabatic decompression and the composition and mean properties of mid-ocean ridge basalts. *Journal of Petrology*, 42, 963-998.
- Beattie, P. (1993). Uranium Thorium Disequilibria and Partitioning on Melting of Garnet Peridotite. *Nature*, 363(6424), 63-65.

1070

Blichert-Toft, J., Albarede, F., and Kornprobst, J. (1999). Lu-Hf isotope systematics of garnet pyroxenites from Beni Bousera, Morocco: Implications for basalt origin. *Science*, 283(5406), 1303-1306. doi: 10.1126/science.283.5406.1303.

1075 Blundy, J. D., and Wood, B. J. (2003). Mineral-melt partitioning of uranium, thorium, and their daughters. In B. Bourdon, G. M. Henderson, C. C. Lundstrom, and S. P. Turner (Eds.), *Uranium-Series Geochemistry* (Vol. 52, pp. 59-123). Mineralogical Society of America.

Bourdon, B., Goldstein, S. J., Bourles, D., Murrell, M. T., and Langmuir, C. H. (2000). Evidence from ¹⁰Be and U series disequilibria on the possible contamination of mid-ocean ridge basalt glasses by sedimentary material. *Geochemistry Geophysics Geosystems*, 1, 2000GC000047.

Bourdon, B., Langmuir, C. H., and Zindler, A. (1996). Ridge-hotspot interaction along the Mid-Atlantic Ridge between 37 degrees 30' and 40 degrees 30'N: The U-Th disequilibrium evidence. *Earth and Planetary Science Letters*, 142(1-2), 175-189.

Bourdon, B., Turner, S. P., Henderson, G. M., and Lundstrom, C. C. (2003). Introduction to U-series Geochemistry. In B. Bourdon, G. M. Henderson, C. C. Lundstrom, and S. P. Turner (Eds.), *Uranium-Series Geochemistry* (Vol. 52, pp. 1-21). Mineralogical Society of America.

1090 Bourdon, B., Turner, S. P., and Ribe, N. M. (2005). Partial melting and upwelling rates beneath the Azores from a U-series isotope perspective. *Earth and Planetary Science Letters*, 239, 42-56.

Bourdon, B., Zindler, A., Elliott, T., and Langmuir, C. H. (1996). Constraints on mantle melting at mid-ocean ridges from global U-238-Th-230 disequilibrium data. *Nature*, 384(6606), 231-235.

Brown, E. L., Petersen, K. D., and Leshner, C. E. (2020). Markov chain Monte Carlo inversion of mantle temperature and source composition, with application to Reykjanes Peninsula, Iceland. *Earth and Planetary Science Letters*, 532, 116007.

1100

Cooper, K. M., Goldstein, S. J., Sims, K. W. W., and Murrell, M. T. (2003). Uranium-series chronology of Gorda Ridge volcanism: new evidence from the 1996 eruption. *Earth and Planetary Science Letters*, 206(3-4), 459-475. doi: Pii S0012-821x(02)01083-X.

1105 Downes, H. (2007). Origin and significance of spinel and garnet pyroxenites in the shallow lithospheric mantle: Ultramafic massifs in orogenic belts in Western Europe and NW Africa. *Lithos*, 99, 1-24. doi: 10.1016/j.lithos.2007.05.006.

Elkins, L. J., Bourdon, B., and Lambart, S. (2019). Testing pyroxenite versus peridotite sources for marine basalts using U-series isotopes. *Lithos*, 332-333, 226-244, doi: 210.1016/j.lithos.2019.1002.1011.

Elkins, L. J., Bourdon, B., and Lambart, S. (2023). Corrigendum to “Testing pyroxenite versus peridotite sources for marine basalts using U-series isotopes” *Lithos*, 452-453, 107217, doi: 107210.101016/j.lithos.102023.107217.

1115 Elkins, L. J., Gaetani, G. A., and Sims, K. W. W. (2008). Partitioning of U and Th during garnet pyroxenite partial melting: Constraints on the source of alkaline ocean island basalts. *Earth and Planetary Science Letters*, 265(1-2), 270-286.

Elkins, L. J., Hamelin, C., Blichert-Toft, J., Scott, S. R., Sims, K. W. W., Devey, C., and Pedersen, R. B. (2016). North Atlantic plume-ridge interaction near Jan Mayen Island. *Geochemical Perspectives Letters*, 2, 55-67. doi: 10.7185/geochemlet.1606.

Elkins, L. J., Scott, S. R., Sims, K. W. W., Rivers, E. R., Devey, C. W., Reagan, M., Hamélin, C., and Pedersen, R. (2016). Exploring the role of mantle eclogite at mid-ocean ridges and hotspots: U-series constraints on Jan Mayen Island and the Kolbeinsey Ridge. *Chemical Geology*, 444, 128-140.

Elkins, L. J., Sims, K. W. W., Prytulak, J., Blichert-Toft, J., Elliott, T., Blusztajn, J., Fretzdorff, S., Reagan, M., Haase, K., Humphris, S., and Schilling, J. G. (2014). Melt generation beneath Arctic Ridges: Implications from U decay series disequilibria in the Mohs, Knipovich, and Gakkel Ridges. *Geochimica et Cosmochimica Acta*, 127, 140-170.

- Elkins, L. J., Sims, K. W. W., Prytulak, J., Mattielli, N., Elliott, T., Blichert-Toft, J., Blusztajn, J., Dunbar, N., Devey, C. W., Mertz, D. F., and Schilling, J. G. (2011). Understanding melt generation beneath the slow spreading Kolbeinsey Ridge from ^{238}U , ^{230}Th , and ^{231}Pa excesses. *Geochimica et Cosmochimica Acta*, 75(21), 6300-6329. doi: 10.1016/j.gca.2011.08.020.
- 1135
- Elkins, L. J., and Spiegelman, M. (2021). pyUserCalc: A revised Jupyter notebook calculator for uranium-series disequilibria in basalts. *Earth and Space Science*, 8(12), e2020EA001619.
- Fabbrizio, A., Schmidt, M. W., Günther, D., and Eikenberg, J. (2009). Experimental determination of Ra mineral/melt partitioning for feldspars and ^{226}Ra -disequilibrium crystallization ages of plagioclase and alkali-feldspar. *Earth and Planetary Science Letters*, 280(1-4), 137-148.
- 1140
- Gale, A., Dalton, C. A., Langmuir, C. H., Su, Y., and Schilling, J. G. (2013). The mean composition of ocean ridge basalts. *Geochemistry Geophysics Geosystems*, 14(3), 489-518. doi: 10.1029/2012GC004334.
- 1145
- Gale, A., Langmuir, C. H., and Dalton, C. A. (2014). The global systematics of ocean ridge basalts and their origin. *Journal of Petrology*, 55(6), 1051-1082.
- Ghiorso, M. S., Hirschmann, M. M., Reiners, P. W., and Kress, V. C. (2002). The pMELTS: A revision of MELTS for improved calculation of phase relations and major element partitioning related to partial melting of the mantle to 3 GPa. *Geochemistry, Geophysics, Geosystems*, 3(5), 1-35.
- 1150
- Goldstein, S. J., Murrell, M. T., and Jacecky, D. R. (1989). Th and U isotopic systematics of basalts from the Juan de Fuca and Gorda Ridges by mass spectrometry. *Earth and Planetary Science Letters*, 96, 134-146.
- 1155
- Goldstein, S. J., Murrell, M. T., Janecky, D. R., Delaney, J. R., and Clague, D. A. (1992). Geochronology and Petrogenesis of Morb from the Juan-De-Fuca and Gorda Ridges by U-238 Th-230 Disequilibrium. *Earth and Planetary Science Letters*, 109(1-2), 255-272.
- 1160
- Goldstein, S. J., Murrell, M. T., and Williams, R. W. (1993). Pa-231 and Th-230 Chronology of Midocean Ridge Basalts. *Earth and Planetary Science Letters*, 115(1-4), 151-159.

- 1165 Hauri, E. H., Wagner, T. P., and Grove, T. L. (1994). Experimental and Natural Partitioning of Th, U, Pb and Other Trace-Elements between Garnet, Clinopyroxene and Basaltic Melts. *Chemical Geology*, 117(1-4), 149-166.
- Hewitt, I. J. (2010). Modelling melting rates in upwelling mantle. *Earth and Planetary Science Letters*, 300(3), 264-274. doi: 10.1016/j.epsl.2010.10.010
- 1170 Hirschmann, M. M., Kogiso, T., Baker, M. B., and Stolper, E. M. (2003). Alkalic magmas generated by partial melting of garnet pyroxenite. *Geology*, 31(6), 481-484.
- Hirschmann, M. M., and Stolper, E. M. (1996). A possible role for garnet pyroxenite in the origin of the "garnet signature" in MORB. *Contributions to Mineralogy and Petrology*, 124(2), 185-208.
- 1175 Hole, M. J. (2018). Mineralogical and geochemical evidence for polybaric fractional crystallization of continental flood basalts and implications for identification of peridotite and pyroxenite source lithologies. *Earth-Science Reviews*, 176, 51-67.
- 1180 Iwamori, H. (1993). Dynamic disequilibrium melting model with porous flow and diffusion-controlled chemical equilibration. *Earth and Planetary Science Letters*, 114(2-3), 301-313.
- Jull, M., Kelemen, P., and Sims, K. (2002). Consequences of diffuse and channeled porous melt migration on uranium series disequilibria. *Geochimica et Cosmochimica Acta*, 66, 4133-4148.
- 1185 Katz, R. F., and Weatherley, S. M. (2012). Consequences of mantle heterogeneity for melt extraction at mid-ocean ridges. *Earth and Planetary Science Letters*, 335-336, 226-237. doi: 10.1016/j.epsl.2012.04.042.
- 1190 Kelemen, P., Shimizu, N., and Dunn, T. (1993). Relative depletion of niobium in some arc magmas and the continental crust: partitioning of K, Nb, La and Ce during melt-rock reaction in the upper mantle. *Earth and Planetary Science Letters*, 120(3-4), 111-134.

- Kelemen, P. B., Hirth, G., Shimizu, N., Spiegelman, M., and Dick, H. J. B. (1997). A review of melt migration processes in the adiabatically upwelling mantle beneath oceanic spreading ridges. *Philosophical Transactions of the Royal Society of London Series a-Mathematical Physical and Engineering Sciences*, 355(1723), 283-318.
- 1195
- Klein, E. M., and Langmuir, C. H. (1987). Global Correlations of Ocean Ridge Basalt Chemistry with Axial Depth and Crustal Thickness. *Journal of Geophysical Research-Solid Earth and Planets*, 92(B8), 8089-8115.
- Klemme, S., Günther, D., Hametner, K., Prowatke, S., and Zack, T. (2006). The partitioning of trace elements between ilmenite, ulvospinel, armalcolite and silicate melts with implications for the early differentiation of the moon. *Chemical Geology*, 234(3), 251-263.
- 1200
- Kogiso, T., Hirose, K., and Takahashi, E. (1998). Melting experiments on homogeneous mixtures of peridotite and basalt: application to the genesis of ocean island basalts. *Earth and Planetary Science Letters*, 162, 45-61, doi:10.1016/S0012-1821X(1098)00156-00153.
- 1205
- Kogiso, T., Hirschmann, M. M., and Frost, D. J. (2003). High-pressure partial melting of garnet pyroxenite: possible mafic lithologies in the source of ocean island basalts. *Earth and Planetary Science Letters*, 216(4), 603-617. doi: 10.1016/S0012-821x(03)00538-7.
- 1210
- Kogiso, T., Hirschmann, M. M., and Pertermann, M. (2004). High-pressure partial melting of mafic lithologies in the mantle. *Journal of Petrology*, 45(12), 2407-2422. Doi: 10.1093/Petrology/Egh057.
- 1215
- Kogiso, T., Hirschmann, M. M., and Reiners, P. W. (2004). Length scales of mantle heterogeneities and their relationship to ocean island basalt geochemistry. *Geochimica et Cosmochimica Acta*, 68(2), 345-360.
- Kokfelt, T. F., Hoernle, K., and Hauff, F. (2003). Upwelling and melting of the Iceland plume from radial variation of U-238-Th-230 disequilibria in postglacial volcanic rocks. *Earth and Planetary Science Letters*, 214(1-2), 167-186. doi: 10.1016/S0012-821x(03)00306-6.
- 1220

Koornneef, J. M., Stracke, A., Bourdon, B., and Gronvold, K. (2012). The influence of source heterogeneity on the U-Th-Pa-Ra disequilibria in post-glacial tholeiites from Iceland. *Geochimica et Cosmochimica Acta*, 87, 243-266. doi: 10.1016/J.Gca.2012.03.041.

1225

Koornneef, J. M., Stracke, A., Bourdon, B., Meier, M. A., Jochum, K. P., Stoll, B., and Grönvold, K. (2012). Melting of a two-component source beneath Iceland. *Journal of Petrology*, 53, 127-157, doi: 110.1093/petrology/egr1059.

1230 Krein, S. B., Behn, M. D., and Grove, T. L. (2020). Origins of major element, trace element, and isotope garnet signatures in mid-ocean ridge basalts. *Journal of Geophysical Research: Solid Earth*, 125(12), doi: e2020JB019612.

1235 La Tourette, T. Z., Kennedy, A. K., and Wasserburg, G. J. (1993). Thorium-uranium fractionation by garnet: Evidence for a deep source and rapid rise of oceanic basalts. *Science*, 261, 729-742.

Lambart, S. (2017). No direct contribution of recycled crust in Icelandic basalts. *Geochemical Perspectives Letters*, 4, 7-12. doi: 10.7185/geochemlet.1728.

1240 Lambart, S., Baker, M. B., and Stolper, E. M. (2016). The role of pyroxenite in basalt genesis: Melt-PX, a melting parameterization for mantle pyroxenites between 0.9 and 5 GPa. *Journal of Geophysical Research: Solid Earth*, 121(8), 5708-5735. doi:10.1002/2015JB012762.

1245 Lambart, S., Koornneef, J. M., Millet, M. A., and Lissenberg, C. J. (2019). Highly heterogeneous depleted mantle recorded in the lower oceanic crust. *Nature Geoscience*, 12(6), 482-486.

Lambart, S., Laporte, D., Provost, A., and Schiano, P. (2012). Fate of Pyroxenite-derived Melts in the Peridotitic Mantle: Thermodynamic and Experimental Constraints. *Journal of Petrology*, 53(3), 451-476. doi: 10.1093/petrology/egr068.

1250

Lambart, S., Laporte, D., and Schiano, P. (2009). An experimental study of pyroxenite partial melts at 1 and 1.5GPa: Implications for the major-element composition of Mid-Ocean Ridge Basalts. *Earth and Planetary Science Letters*, 288(1), 335-347. doi: 10.1016/j.epsl.2009.09.038.

1255 Lambart, S., Laporte, D., and Schiano, P. (2013). Markers of the pyroxenite contribution in the major-element compositions of oceanic basalts: Review of the experimental constraints. *Lithos*, 160-161, 14-36. doi: 10.1016/j.lithos.2012.11.018.

Landwehr, D., Blundy, J., Chamorro-Perez, E. M., Hill, E., and Wood, B. (2001). U-series disequilibria generated
1260 by partial melting of spinel lherzolite. *Earth and Planetary Science Letters*, 188(3-4), 329-348.

Lang, O. I., and Lambart, S. (2022). First-row transition elements in pyroxenites and peridotites: A promising tool for constraining mantle source mineralogy. *Chemical Geology*, 612, 121137.

1265 Langmuir, C., Klein, E. M., and Plank, T. (1992). Petrological systematics of mid-ocean ridge basalts: constraints on melt generation beneath ocean ridges. In *Mantle Flow and Melt Generation at Mid-Ocean Ridges* (pp. 183-280).
Le Roux, V., Lee, C. T., and Turner, S. J. (2010). Zn/Fe systematics in mafic and ultramafic systems: Implications for detecting major element heterogeneities in the Earth's mantle. *Geochimica et Cosmochimica Acta*, 74(9), 2779-2796.

1270

Liang, Y. (2008). Simple models for dynamic melting in an upwelling heterogeneous mantle column: analytical solutions. *Geochimica et Cosmochimica Acta*, 72(15), 3804-3821.

Liang, Y., and Parmentier, E. M. (2010). A two-porosity double lithology model for partial melting, melt transport
1275 and melt-rock reaction in the mantle: mass conservation equations and trace element transport. *Journal of Petrology*, 51(1-2), 125-152.

Lin, J., Purdy, G. M., Schouten, H., Sempere, J.-C., and Zervas, C. (1990). Evidence from gravity data for focused magmatic accretion along the Mid-Atlantic Ridge. *Nature*, 344, 627-632.

1280

Lundstrom, C. (2000). Models of U-series disequilibria generation in MORB: the effects of two scales of melt porosity. *Physics of the Earth and Planetary Interiors*, 121(3-4), 189-204.

1285 Lundstrom, C. C. (2003). Uranium-series disequilibria in mid-ocean ridge basalts: observations and models of basalt genesis. *Reviews in Mineralogy and Geochemistry*, 52(1), 175-214.

Lundstrom, C. C., Gill, J., Williams, Q., and Hanan, B. B. (1998). Investigating solid mantle upwelling beneath mid-ocean ridges using U-series disequilibria. II. A local study at 33 degrees Mid-Atlantic Ridge. *Earth and Planetary Science Letters*, 157(3-4), 167-181.

1290

Lundstrom, C. C., Gill, J., Williams, Q., and Perfit, M. R. (1995). Mantle Melting and Basalt Extraction by Equilibrium Porous Flow. *Science*, 270(5244), 1958-1961.

1295 Lundstrom, C. C., Sampson, D. E., Perfit, M. R., Gill, J., and Williams, Q. (1999). Insights into mid-ocean ridge basalt petrogenesis: U-series disequilibria from the Siqueiros Transform, Lamont Seamounts, and East Pacific Rise. *Journal of Geophysical Research-Solid Earth*, 104(B6), 13035-13048.

Mallik, A., Lambart, S., and Chin, E. J. (2021). Tracking the evolution of magmas from heterogeneous mantle sources to eruption. *Mantle Convection and Surface Expressions*, 151-177.

1300

McDade, P., Blundy, J. D., and Wood, B. J. (2003). Trace element partitioning on the Tinaquillo Lherzolite solidus at 1.5 GPa. *Physics of the Earth and Planetary Interiors*, 139(1-2), 129-147.

1305 McKenzie, D. (1985). Th-230-U-238 Disequilibrium and the Melting Processes beneath Ridge Axes. *Earth and Planetary Science Letters*, 72(2-3), 149-157.

McKenzie, D., and Bickle, M. (1988). The volume and composition of melt generated by extension of the lithosphere. *Journal of Petrology*, 29(3), 625-679.

1310 McKenzie, D., and O'Nions, R. (1991). Partial Melt Distributions From Inversion Of Rare-Earth Element Concentrations. *Journal of Petrology*, 32, 1021.

- 1315 Millet, M. A., Doucelance, R., Schiano, P., David, K., and Bosq, C. (2008). Mantle plume heterogeneity versus shallow-level interactions: a case study, the São Nicolau Island, Cape Verde archipelago. *Journal of Volcanology and Geothermal Research*, 176(2), 265-276.
- Montesi, L. G., Behn, M. D., Hebert, L. B., Lin, J., and Barry, J. L. (2011). Controls on melt migration and extraction at the ultraslow Southwest Indian Ridge 10-16 E. *Journal of Geophysical Research: Solid Earth*, 116, B10.
- 1320 Montesi, L. G. J., and Behn, M. D. (2007). Mantle flow and melting underneath oblique and ultraslow mid-ocean ridges. *Geophysical Research Letters*, 34(24), L24307. doi: 10.1029/2007gl031067.
- 1325 Neave, D. A., Namur, O., Shorttle, O., and Holtz, F. (2019). Magmatic evolution biases basaltic records of mantle chemistry towards melts from recycled sources. *Earth and Planetary Science Letters*, 520, 199-211.
- Niu, Y., and Hékinian, R. (1997). Basaltic liquids and harzburgitic residues in the Garrett Transform: a case study at fast-spreading ridges. *Earth and Planetary Science Letters*, 146(1), 243-258.
- 1330 Peate, D. W., Hawkesworth, C. J., van Calsteren, P. W., Taylor, R. N., and Murton, B. J. (2001). U-238-Th-230 constraints on mantle upwelling and plume-ridge interaction along the Reykjanes Ridge. *Earth and Planetary Science Letters*, 187(3-4), 259-272.
- 1335 Pertermann, M., and Hirschmann, M. (2003). Partial melting experiments on MORB-like pyroxenite between 2 and 3 GPa: Constraints on the presence of pyroxenite in basalt source regions from solidus location and melting rate. *Journal of Geophysical Research*, 108. doi: 10.1029/2000JB000118.
- 1340 Pertermann, M., and Hirschmann, M. M. (2003). Anhydrous partial melting experiments on MORB-like eclogite: Phase relations, phase compositions and mineral-melt partitioning of major elements at 2-3 GPa. *Journal of Petrology*, 44(12), 2173-2201. doi: 10.1093/Petrology/Egg074.

Pertermann, M., Hirschmann, M. M., Hametner, K., Gunther, D., and Schmidt, M. W. (2004). Experimental determination of trace element partitioning between garnet and silica-rich liquid during anhydrous partial melting of MORB-like eclogite. *Geochemistry Geophysics Geosystems*, 5, Q05A01. doi: 10.1029/2003gc000638.

1345

Plank, T., and Langmuir, C. H. (1992). Effects of the melting regime on the composition of oceanic crust. *Journal of Geophysical Research*, 97, 19749-19770.

1350 Plank, T., Spiegelman, M., Langmuir, C. H., and Forsyth, D. W. (1995). The meaning of ‘mean F’: clarifying the mean extent of melting at ocean ridges. *Journal of Geophysical Research*, 100, 15045-15052.

Prytulak, J., and Elliott, T. (2007). TiO₂ enrichment in ocean island basalts. *Earth and Planetary Science Letters*, 263(3-4), 388-403.

1355 Prytulak, J., and Elliott, T. (2009). Determining melt productivity of mantle sources from U-238-Th-230 and U-235-Pa-231 disequilibria; an example from Pico Island, Azores. *Geochimica et Cosmochimica Acta*, 73(7), 2103-2122. doi: 10.1016/J.Gca.2009.01.001.

1360 Reagan, M., Turner, S., Handley, H., Turner, M., Beier, C., Caulfield, J., and Peate, D. (2017). ²¹⁰Pb-²²⁶Ra disequilibria in young gas-laden magmas. *Scientific Reports*, 7, 45186.

Reagan, M. K., and Sims, K. W. W. (2001). Are Melt Migration Rates Through the Mantle Universally Rapid? *AGU Fall Meeting Abstracts, 2001*, V51E-09.

1365 Richardson, C., and McKenzie, D. (1994). Radioactive disequilibria from 2D models of melt generation by plumes and ridges. *Earth and Planetary Science Letters*, 128(3-4), 425-437.

Rubin, K. H., van der Zander, I., Smith, M. C., and Bergmanis, E. C. (2005). Minimum speed limit for ocean ridge magmatism from Pb-210-Ra-226-Th-230 disequilibria. *Nature*, 437(7058), 534-538. doi: 10.1038/Nature03993.

1370

Rudge, J. F., Maclennan, J., and Stracke, A. (2013). The geochemical consequences of mixing melts from a heterogeneous mantle. *Geochimica et Cosmochimica Acta*, 114, 112-143.

- 1375 Russo, C. J., Rubin, K. H., and Graham, D. W. (2009). Mantle melting and magma supply to the Southeast Indian Ridge: The roles of lithology and melting conditions from U-series disequilibria. *Earth and Planetary Science Letters*, 278(1-2), 55-66. doi: 10.1016/J.Epsl.2008.11.016.
- 1380 Salters, V. J., and Dick, H. J. (2002). Mineralogy of the mid-ocean-ridge basalt source from neodymium isotopic composition of abyssal peridotites. *Nature*, 418(6893), 68.
- Salters, V. J., and Stracke, A. (2004). Composition of the depleted mantle. *Geochemistry, Geophysics, Geosystems*, 5(5).
- 1385 Salters, V. J. M., and Longhi, J. (1999). Trace element partitioning during the initial stages of melting beneath mid-ocean ridges. *Earth and Planetary Science Letters*, 166(1-2), 15-30.
- Salters, V. J. M., Longhi, J. E., and Bizimis, M. (2002). Near mantle solidus trace element partitioning at pressures up to 3.4 GPa. *Geochemistry Geophysics Geosystems*, 3(7), 1038. doi: 10.1029/2001GC000148.
- 1390 Schiano, P., Birck, J. L., and Allègre, C. J. (1997). Osmium-strontium-neodymium-lead isotopic covariations in mid-ocean ridge basalt glasses and the heterogeneity of the upper mantle. *Earth and Planetary Science Letters*, 150(3), 363-379.
- 1395 Scott, S. R., Ramos, F. C., and Gill, J. B. (2018). Spreading dynamics of an intermediate ridge: Insights from U-series disequilibria, Endeavour Segment, Juan de Fuca Ridge. *Journal of Petrology*, 59, 1847-1868, doi: 10.1093/petrology/egy082.
- 1400 Shen, Y., and Forsyth, D. W. (1995). Geochemical Constraints on Initial and Final Depths of Melting beneath Midocean Ridges. *Journal of Geophysical Research-Solid Earth*, 100(B2), 2211-2237.
- Shorttle, O., and MacLennan, J. (2011). Compositional trends of Icelandic basalts: Implications for short-length scale lithological heterogeneity in mantle plumes. *Geochem. Geophys. Geosyst.*, 12. doi: 10.1029/2011gc003748.

Shorttle, O., Maclennan, J., and Lambart, S. (2014). Quantifying lithological variability in the mantle. *Earth and Planetary Science Letters*, 395, 24-40.

1405

Sims, K. W. W., DePaolo, D. J., Murrell, M. T., Baldrige, W. S., Goldstein, S., Clague, D., and Jull, M. (1999). Porosity of the melting zone and variations in the solid mantle upwelling rate beneath Hawaii: Inferences from U-238-Th-230-Ra-226 and U-235-Pa-231 disequilibria. *Geochimica et Cosmochimica Acta*, 63(23-24), 4119-4138.

1410

Sims, K. W. W., Goldstein, S. J., Blichert-Toft, J., Perfit, M. R., Kelemen, P., Fornari, D. J., Michael, P., Murrell, M. T., Hart, S. R., DePaolo, D. J., Layne, G., Ball, L., Jull, M., and Bender, J. (2002). Chemical and isotopic constraints on the generation and transport of magma beneath the East Pacific Rise. *Geochimica et Cosmochimica Acta*, 66(19), 3481-3504.

1415

Sobolev, A. V., Hofmann, A. W., Brüggemann, G., Batanova, V. G., and Kuzmin, D. V. (2008). A quantitative link between recycling and osmium isotopes. *Science*, 321(5888), 536-536.

Soderman, C. R., Shorttle, O., Matthews, S., and Williams, H. M. (2022). Global trends in novel stable isotopes in basalts: Theory and observations. *Geochimica et Cosmochimica Acta*, 318, 388-414.

1420

Spiegelman, M. (2000). UserCalc: a web-based uranium series calculator for magma migration problems. *Geochemistry Geophysics Geosystems*, 1(8), 1016. doi: 10.1029/1999GC000030.

Spiegelman, M., and Elliott, T. (1993). Consequences of Melt Transport for Uranium Series Disequilibrium in Young Lavas. *Earth and Planetary Science Letters*, 118(1-4), 1-20.

1425

Spiegelman, M., Kelemen, P., and Aharonov, E. (2001). Causes and consequences of flow organization during melt transport: The reaction infiltration instability in compactible media. *Journal of Geophysical Research: Solid Earth*, 106(B2), 2061-2077. doi:10.1029/2000JB900240.

1430

Spiegelman, M., and Kelemen, P. B. (2003). Extreme chemical variability as a consequence of channelized melt transport. *Geochem. Geophys. Geosyst.*, 4(7), 1055. doi: 10.1029/2002GC000336.

- 1435 Spiegelman, M., and Kenyon, P. (1992). The requirements for chemical disequilibrium during magma migration. *Earth and Planetary Science Letters*, 109(3-4), 611-620.
- Standish, J. J., and Sims, K. W. W. (2010). Young off-axis volcanism along the ultraslow-spreading Southwest Indian Ridge. *Nature Geoscience*, 3, 286-292.
- 1440 Stolper, E. M., and Asimow, P. D. (2007). Insights into mantle melting from graphical analysis of one-component systems. *Am Journal Sci*, 307, 1051-1139.
- Stracke, A., and Bourdon, B. (2009). The importance of melt extraction for tracing mantle heterogeneities. *Geochimica et Cosmochimica Acta*, 73, 218-238.
- 1445 Stracke, A., Bourdon, B., and McKenzie, D. (2006). Melt extraction in the Earth's mantle: Constraints from U-Th-Pa-Ra studies in oceanic basalts. *Earth and Planetary Science Letters*, 244(1-2), 97-112. doi: 10.1016/J.Epsl.2006.01.057.
- 1450 Sun, C., Graff, M., and Liang, Y. (2017). Trace element partitioning between plagioclase and silicate melt: The importance of temperature and plagioclase composition, with implications for terrestrial and lunar magmatism. *Geochimica et Cosmochimica Acta*, 206, 273-295, doi: 10.1016/j.gca.2017.03.003.
- 1455 Tepley, F. J., Lundstrom, C. C., Sims, K. W. W., and Hekinian, R. (2004). U-series disequilibria in MORB from the Garrett Transform and implications for mantle melting. *Earth and Planetary Science Letters*, 223(1-2), 79-97.
- Turner, S., Kokfelt, T., Hauff, F., Haase, K., Lundstrom, C., Hoernle, K., Yeo, I. A., and Devey, C. (2015). Mid-ocean ridge basalt generation along the slow-spreading, South Mid-Atlantic Ridge (5-11°S): Inferences from ²³⁸U-²³⁰Th-²²⁶Ra disequilibria. *Geochimica et Cosmochimica Acta*, 169, 152-166.
- 1460 Turner, S., Kokfelt, T., Hoernle, K., Lundstrom, C., and Hauff, F. (2016). ²³¹Pa systematics in postglacial volcanic rocks from Iceland. *Geochimica et Cosmochimica Acta*, 185, 129-140.

- 1465 Van Westrenen, W., Blundy, J. D., and Wood, B. J. (1999). Crystal-chemical controls on trace element partitioning between garnet and anhydrous silicate melt. *American Mineralogist*, 84 (5-6), 838-847.
- 1470 Waters, C. L., Sims, K. W. W., Perfit, M. R., Blichert-Toft, J., and Blusztajn, J. (2011). Perspective on the genesis of E-MORB from chemical and isotopic heterogeneity at 9°-10°N East Pacific Rise. *Journal of Petrology*, 52, 565-602. doi: 10.1093/petrology/egq091.
- 1475 Waters, C. L., Sims, K. W. W., Soule, S. A., Blichert-Toft, J., Dunbar, N. W., Plank, T., Prytulak, J., Sohn, R. A., and Tivey, M. A. (2013). Recent volcanic accretion at 9°N-10°N East Pacific Rise as resolved by combined geochemical and geological observations. *Geochemistry Geophysics Geosystems*, 14(8), 2547–2574. doi: 10.1002/ggge.20134.
- 1480 Weatherley, S. M., and Katz, R. F. (2012). Melting and channelized magmatic flow in chemically heterogeneous, upwelling mantle. *Geochem. Geophys. Geosyst.*, 13(1), Q0AC18. doi: 10.1029/2011GC003989.
- Williams, R. W., and Gill, J. B. (1989). Effects of Partial Melting on the Uranium Decay Series. *Geochimica et Cosmochimica Acta*, 53(7), 1607-1619.
- 1485 Workman, R. K., Hart, S. R., Jackson, M., Regelous, M., Farley, K., Blusztajn, J., Kurz, M., and Staudigel, H. (2004). Recycled metasomatized lithosphere as the origin of the Enriched Mantle II (EM2) end-member: Evidence from the Samoan Volcanic Chain. *Geochemistry, Geophysics, Geosystems*, 5(4).
- 1490 Yang, S., Humayun, M., and Salters, V. J. (2020). Elemental constraints on the amount of recycled crust in the generation of mid-oceanic ridge basalts (MORBs). *Science advances*, 6(26), eaba2923.
- Yang, Z. F., Li, J., Jiant, Q. B., Xu, F., Guo, S. Y., Li, Y., and Zhang, J. (2019). Using major element log ratios to recognize compositional patterns of basalt: Implications for source lithological and compositional heterogeneities. *Journal of Geophysical Research: Solid Earth*, 124(4), 3458-3490.
- Zou, H. (2007). *Quantitative Geochemistry*. Imperial College Press.

1495 Zou, H., and Zindler, A. (2000). Theoretical studies of ^{238}U - ^{230}Th - ^{226}Ra and ^{235}U - ^{231}Pa disequilibria in young lavas produced by mantle melting. *Geochimica et Cosmochimica Acta*, 64(10), 1809-1817.

Tables

Table 1. Model run matrix for this study. Uranium-series activity ratios were determined in partial melts for all of the scenarios listed, for solid mantle upwelling rates (W_0) ranging from 0.5 to 50 cm/yr., maximum residual mass porosities (ϕ_0) of 0.1 to 2.0%, and chemical equilibrium, chemical disequilibrium, and intermediate transport models, with Damköhler numbers (Da) of infinity, 0, and 0.1, respectively.

T_p (°C)	P_{Lithos} (kbar)	Pyroxenite type	Pyroxenite %	Peridotite %	T_p (°C)	P_{Lithos} (kbar)	Pyroxenite type	Pyroxenite %	Peridotite %
1300	5.1	G2	1	99	1400	5.1	G2	1	99
1300	5.1	G2	5	95	1400	5.1	G2	5	95
1300*	5.1	G2	10	90	1400*	5.1	G2	10	90
1300	5.1	G2	20	80	1400	5.1	G2	20	80
1300	5.1	G2	50	50	1400	5.1	G2	50	50
1300	5.1	KG1	1	99	1400	5.1	KG1	1	99
1300	5.1	KG1	5	95	1400	5.1	KG1	5	95
1300	5.1	KG1	10	90	1400	5.1	KG1	10	90
1300	5.1	KG1	20	80	1400	5.1	KG1	20	80
1300	5.1	KG1	50	50	1400	5.1	KG1	50	50
1300	5.1	m7-16	1	99	1400	5.1	m7-16	1	99
1300	5.1	m7-16	5	95	1400	5.1	m7-16	5	95
1300	5.1	m7-16	10	90	1400*	5.1	m7-16	10	90
1300	5.1	m7-16	20	80	1400	5.1	m7-16	20	80
1300	5.1	m7-16	50	50	1400	5.1	m7-16	50	50
1300	5.1	MIX1G	1	99	1400	5.1	MIX1G	1	99
1300	5.1	MIX1G	5	95	1400	5.1	MIX1G	5	95
1300*, a,b	5.1	MIX1G	10	90	1400*, b	5.1	MIX1G	10	90
1300	5.1	MIX1G	20	80	1400	5.1	MIX1G	20	80
1300	5.1	MIX1G	50	50	1400	5.1	MIX1G	50	50
1200 ^c	5.1	none	0	100					
1200 ^c	2.2	none	0	100					
1300 ^c	5.1	none	0	100					
1300 ^c	2.2	none	0	100					
1400	5.1	none	0	100					
1400	3.3	none	0	100					

^a In addition to the default conditions, the effects of radioactive decay due to aging during lithospheric transport of extracted magma were determined, using a transport rate of 15 m/yr.

^b In addition to default conditions, the effects of integration over a two-dimensional, triangular melting regime were determined for an upwelling rate of 3 cm/yr., a residual maximum porosity of 0.8%, and extracted magma transport rates between 1 and 100,000 cm/yr.

^c Additional calculations were conducted for these scenarios using alternative U and Th partitioning after Sun et al. (2017) and Krein et al. (2021).

* Stable trace element concentrations were additionally determined for selected scenarios, as described in the text.

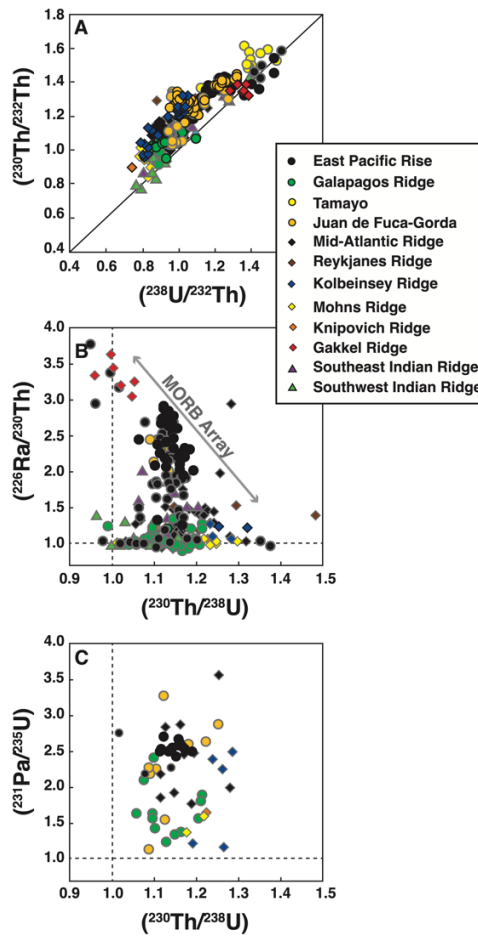
Table 2. Default mineral/melt partition coefficients (D_i) used to calculate bulk rock partition coefficients in model calculations for this study.

Lithology	Phase	D_U	D_{Th}	D_{Pa}^*	D_{Ra}^*	Reference
<u>Garnet peridotite,</u> <u>KG1 pyroxenite</u>	Garnet	0.038	0.017	0.00001	0.00001	RD 1097-5 experiment, Salters et al. (2002)
	Clinopyroxene	0.0030	0.0040	0.00001	0.00001	RD 1097-5 experiment, Salters et al. (2002)
	Olivine	0.00005	0.00047	0.00001	0.00001	RD 1097-5 experiment, Salters et al. (2002)
	Orthopyroxene	0.0078	0.0086	0.00001	0.00001	TM0500-3 experiment, Salters et al. (2002)
	Pigeonite	0.00050	0.00018	0.00001	0.00001	W&P 122-1 experiment, Landwehr et al. (2001)
	Spinel	0.012	0.0024	0.00001	0.00001	Lunar basalt, Klemme et al. (2006)
<u>Spinel peridotite</u>	Clinopyroxene	0.0080	0.0070	0.00001	0.00001	TM 1094-9 experiment, Salters and Longhi (1999)
	Olivine	0.00005	0.00047	0.00001	0.00001	RD 1097-5 experiment, Salters et al. (2002)
	Orthopyroxene	0.0024	0.0027	0.00001	0.00001	RD 1097-2 experiment, Salters et al. (2002)
	Plagioclase ^a	0.0006	0.0034	0.00001	0.02000	D_U, D_{Th} calculated after Blundy and Wood (2003); D_{Ra} from Fabbrizio et al. (2009)
	Pigeonite	0.0005	0.00018	0.00001	0.00001	W&P 122-1 experiment, Landwehr et al. (2001)
	Spinel	0.012	0.0024	0.00001	0.00001	Lunar basalt, Klemme et al. (2006)
<u>G2 pyroxenite</u>	Garnet	0.02405	0.00415	0.00001	0.00001	A343 experiment, Pertermann et al. (2004)
	Clinopyroxene	0.0041	0.0032	0.00001	0.00001	A343 experiment, Pertermann et al. (2004)
	Olivine	0.00005	0.00047	0.00001	0.00001	RD 1097-5 experiment, Salters et al. (2002)
	Orthopyroxene	0.0078	0.0086	0.00001	0.00001	TM0500-3 experiment, Salters et al. (2002)
	Plagioclase	0.0006	0.0034	0.00001	0.02000	D_U, D_{Th} calculated after Blundy and Wood (2003); D_{Ra} from Fabbrizio et al. (2009)
	Pigeonite	0.0096	0.010	0.00001	0.00001	18 experiment, Van Westrenen et al. (2000)
<u>MIX1G, m7-16</u> <u>pyroxenite</u>	Garnet	0.013	0.0032	0.00001	0.00001	Experimental results, Elkins et al. (2008)
	Clinopyroxene	0.017	0.015	0.00001	0.00001	Experimental results, Elkins et al. (2008)
	Olivine	0.00005	0.00047	0.00001	0.00001	RD 1097-5 experiment, Salters et al. (2002)
	Spinel	0.046	0.016	0.00001	0.00001	Maximum measured, Elkins et al. (2008)
	Orthopyroxene	0.0078	0.0086	0.00001	0.00001	TM0500-3 experiment, Salters et al. (2002)
	Plagioclase ^a	0.0006	0.0034	0.00001	0.02000	D_U, D_{Th} calculated after Blundy and Wood (2003); D_{Ra} from Fabbrizio et al. (2009)
	Pigeonite	0.0096	0.010	0.00001	0.00001	Experiment 18, Van Westrenen et al. (2000)

* By convention, D_{Pa} and D_{Ra} are set equal to very small values (1×10^{-5}) for most mantle minerals, except D_{Ra} in plagioclase.

** There are no published partitioning data for U, Th, Ra, or Pa in the minerals quartz, kyanite, and coesite, and the mineral/melt partition coefficients in these minerals are expected to be extremely low. To simplify the calculations in this paper, the D_i values for these three minerals are assumed to be zero.

^a Additional calculations were performed for a few peridotite and MIX1G melting scenarios (see text, Table 1) using alternative D_U and D_{Th} values for plagioclase of 0.07 and 0.022, respectively, after Sun et al. (2017) and Krein et al. (2021).



1505

Figure 1. A. $(^{230}\text{Th}/^{232}\text{Th})$ vs. $(^{238}\text{U}/^{232}\text{Th})$ “equiline” diagram after Allègre (1968); B. $(^{226}\text{Ra}/^{230}\text{Th})$ vs. $(^{230}\text{Th}/^{238}\text{U})$ diagram; and C. $(^{231}\text{Pa}/^{235}\text{U})$ vs. $(^{230}\text{Th}/^{238}\text{U})$ diagram showing global MORB mass spectrometry data (Bourdon et al. 1996b, 2000; Cooper et al. 2003; Elkins et al. 2011, 2014, 2016b; Goldstein et al. 1989, 1992, 1993; Kokfelt et al. 2003; Lundstrom et al. 1995, 1998, 1999; Peate et al. 2001; Reagan et al. 2017; Rubin et al. 2005; Russo et al. 2009; Sims et al. 2002; Standish and Sims 2010; Tepley et al. 2004; Turner et al. 2015, 2016; Waters et al. 2011, 2013). Similar to Elkins et al. (2019), the data shown have been filtered to omit samples with evidence for significant alteration due to interaction with seawater or seawater-derived materials, based on $(^{234}\text{U}/^{238}\text{U}) \neq 1.00$ with a filtering criterion of $\pm 1\%$, and to omit those with no U isotope data constraints. Data for samples with known age constraints are illustrated with black outlines, while other data points that lack such

1510

1515 constraints are outlined in gray.

Isolated Peridotite Melting

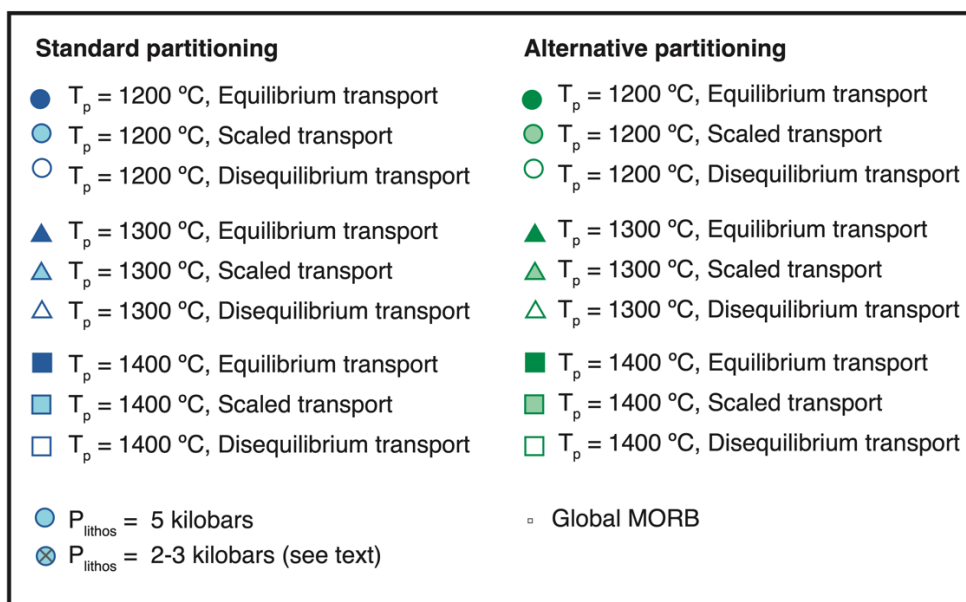
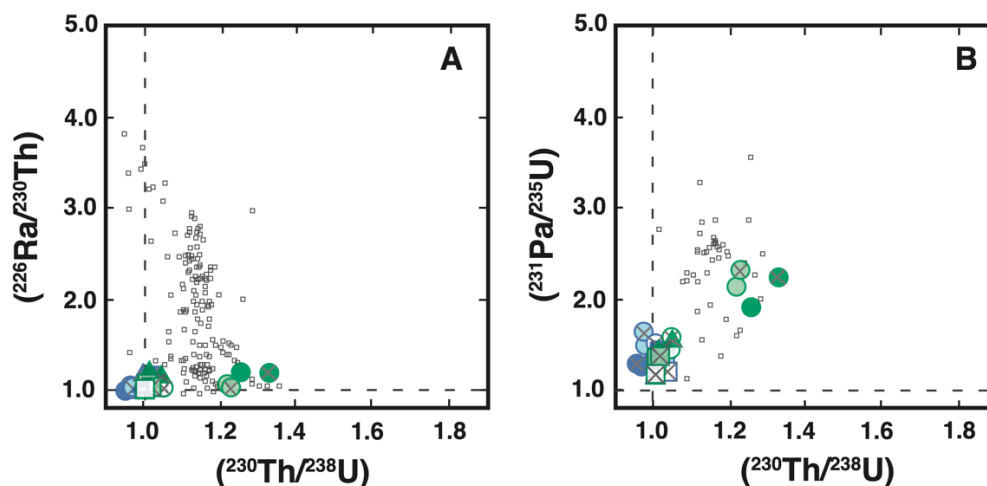
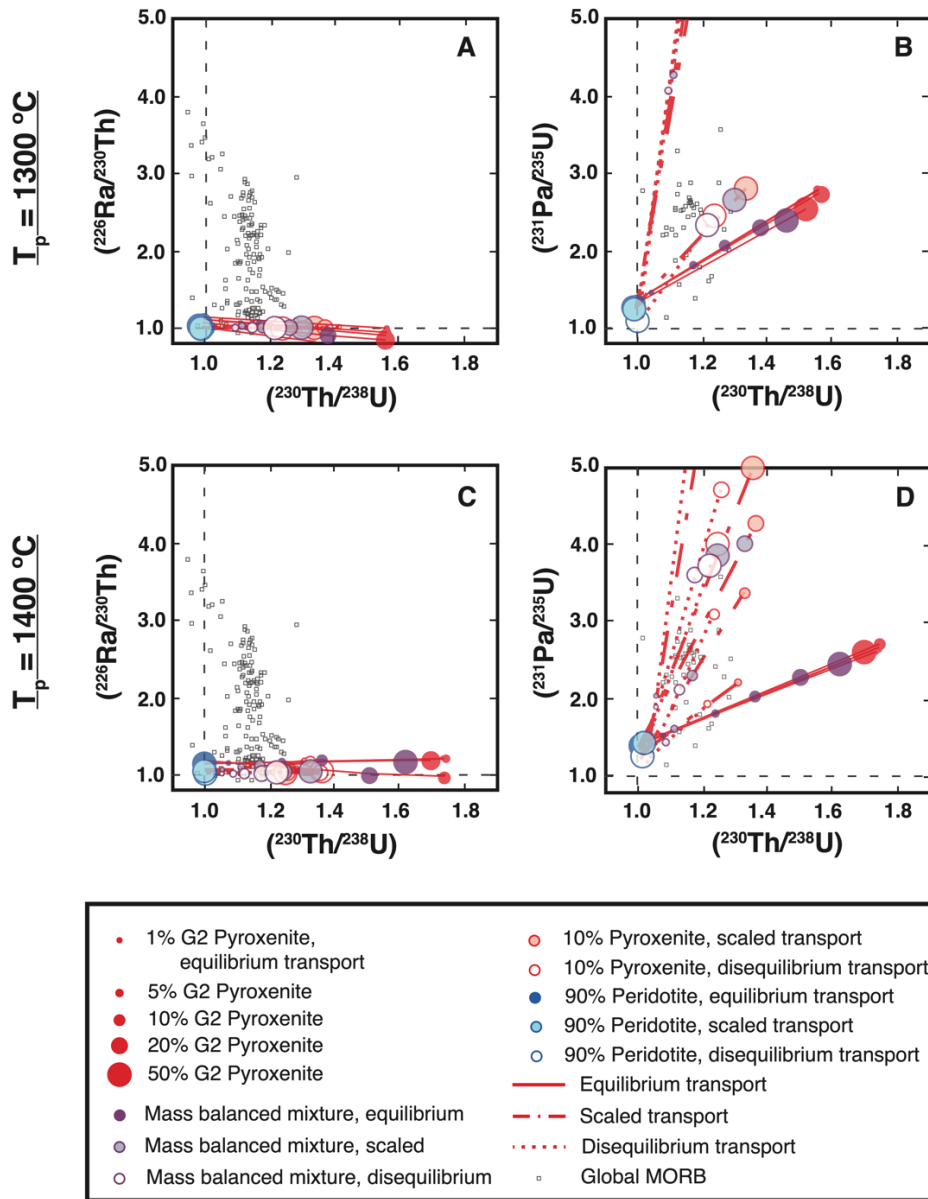


Figure 2. Representative results for pure peridotite melting, showing **A.** $(^{226}\text{Ra}/^{230}\text{Th})$ and **B.** $(^{231}\text{Pa}/^{235}\text{U})$ vs. $(^{230}\text{Th}/^{238}\text{U})$ in partial melts. Results shown have a solid mantle upwelling rate (W_0) of 3 cm/yr. and a residual maximum porosity (ϕ_0) of 0.8%, final melting pressures of 5 kbar as well as alternative lower values (symbols with X's; see text for further explanation), potential temperatures of 1300 and 1400 °C, and both default and alternative proposed partition coefficients (see text). Global MORB compositions are shown using small data points for comparison, after Figure 1.



1525 **Figure 3.** Modeled **A.** $(^{226}\text{Ra}/^{230}\text{Th})$ and **B.** $(^{231}\text{Pa}/^{235}\text{U})$ vs. $(^{230}\text{Th}/^{238}\text{U})$ in partial melt compositions for $T_p = 1300$
 °C, and **C.** $(^{226}\text{Ra}/^{230}\text{Th})$ and **D.** $(^{231}\text{Pa}/^{235}\text{U})$ vs. $(^{230}\text{Th}/^{238}\text{U})$ compositions for $T_p = 1400$ °C, for partial melts of G2
 pyroxenite and coexisting peridotite at a final melting pressure of 5 kbar, as well as mass-balanced binary melt
 mixtures (see text, Table S1), Calculated results are shown for G2 pyroxenite abundances in the solid source of 1
 to 50% and a range of magma transport models, all for a representative set of results using a solid mantle upwelling
 1530 of 3 cm/yr. and a residual maximum porosity of 0.8%. Global MORB data are shown for comparison, after Figures
 1 and 2.

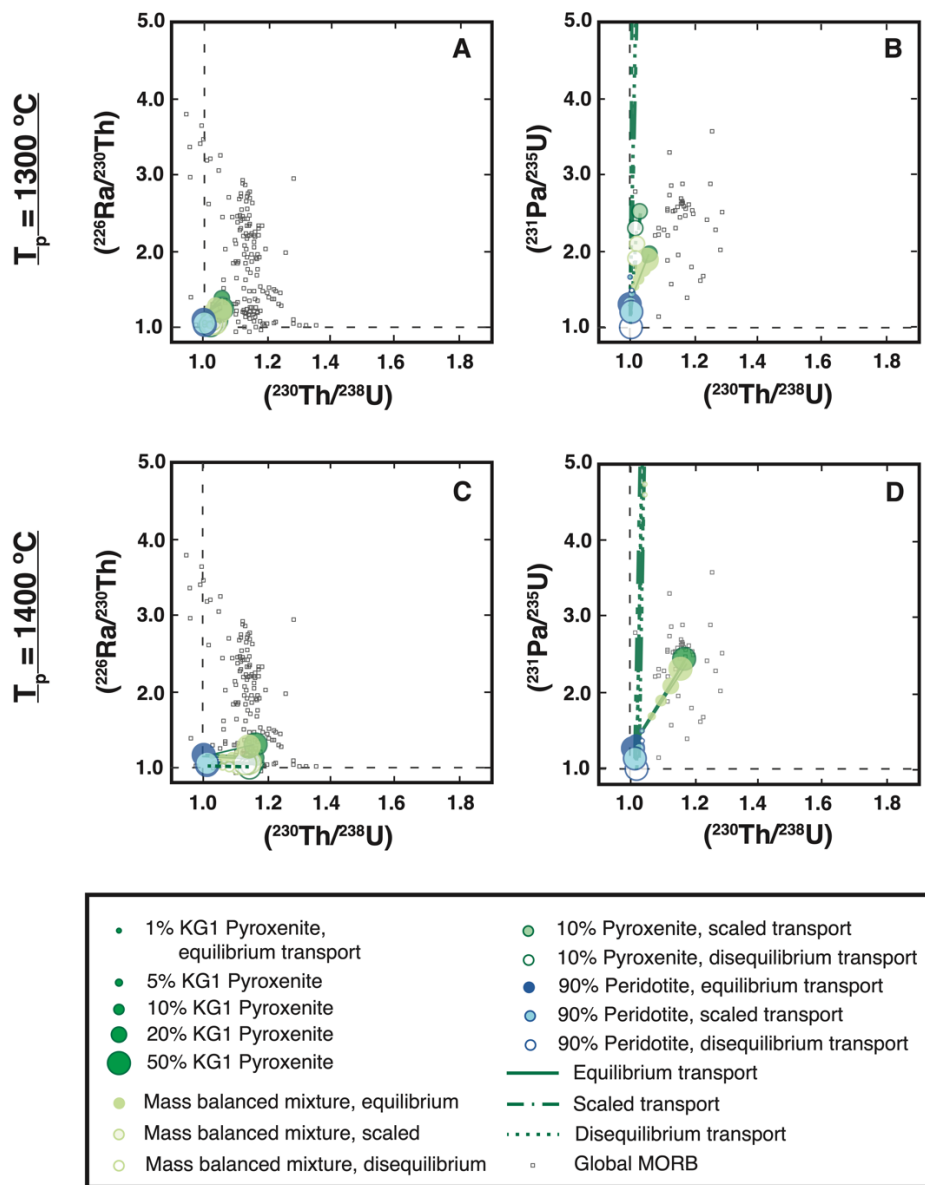


Figure 4. Modeled **A.** $(^{226}\text{Ra}/^{230}\text{Th})$ and **B.** $(^{231}\text{Pa}/^{235}\text{U})$ vs. $(^{230}\text{Th}/^{238}\text{U})$ in partial melt compositions for $T_p = 1300$ °C, and **C.** $(^{226}\text{Ra}/^{230}\text{Th})$ and **D.** $(^{231}\text{Pa}/^{235}\text{U})$ vs. $(^{230}\text{Th}/^{238}\text{U})$ compositions for $T_p = 1400$ °C, for partial melts of KG1 pyroxenite and coexisting peridotite at a final melting pressure of 5 kbar, as well as mass-balanced binary melt mixtures (see text, Table S1), Calculated results are shown for KG1 pyroxenite abundances in the solid source of 1 to 50% and a range of magma transport models, all for a representative set of results using a solid mantle upwelling of 3 cm/yr. and a residual maximum porosity of 0.8%. Global MORB data are shown for comparison, after Figures 1 and 2.

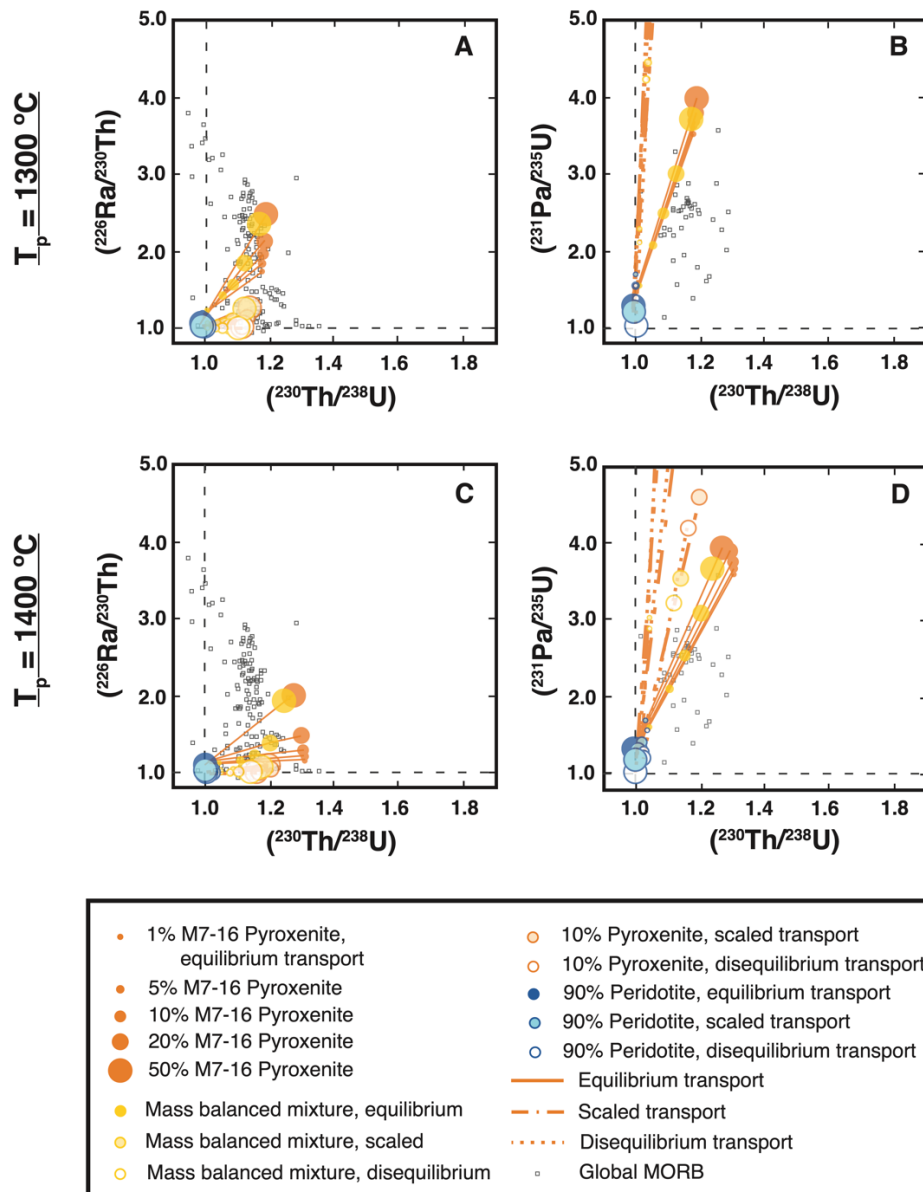


Figure 5. Modeled **A.** $(^{226}\text{Ra}/^{230}\text{Th})$ and **B.** $(^{231}\text{Pa}/^{235}\text{U})$ vs. $(^{230}\text{Th}/^{238}\text{U})$ in partial melt compositions for $T_p = 1300$ °C, and **C.** $(^{226}\text{Ra}/^{230}\text{Th})$ and **D.** $(^{231}\text{Pa}/^{235}\text{U})$ vs. $(^{230}\text{Th}/^{238}\text{U})$ compositions for $T_p = 1400$ °C, for partial melts of M7-16 pyroxenite and coexisting peridotite at a final melting pressure of 5 kbar, as well as mass-balanced binary melt mixtures (see text, Table S1), Calculated results are shown for M7-16 pyroxenite abundances in the solid source of 1 to 50% and a range of magma transport models, all for a representative set of results using a solid mantle upwelling of 3 cm/yr. and a residual maximum porosity of 0.8%. Global MORB data are shown for comparison, after Figures 1 and 2.

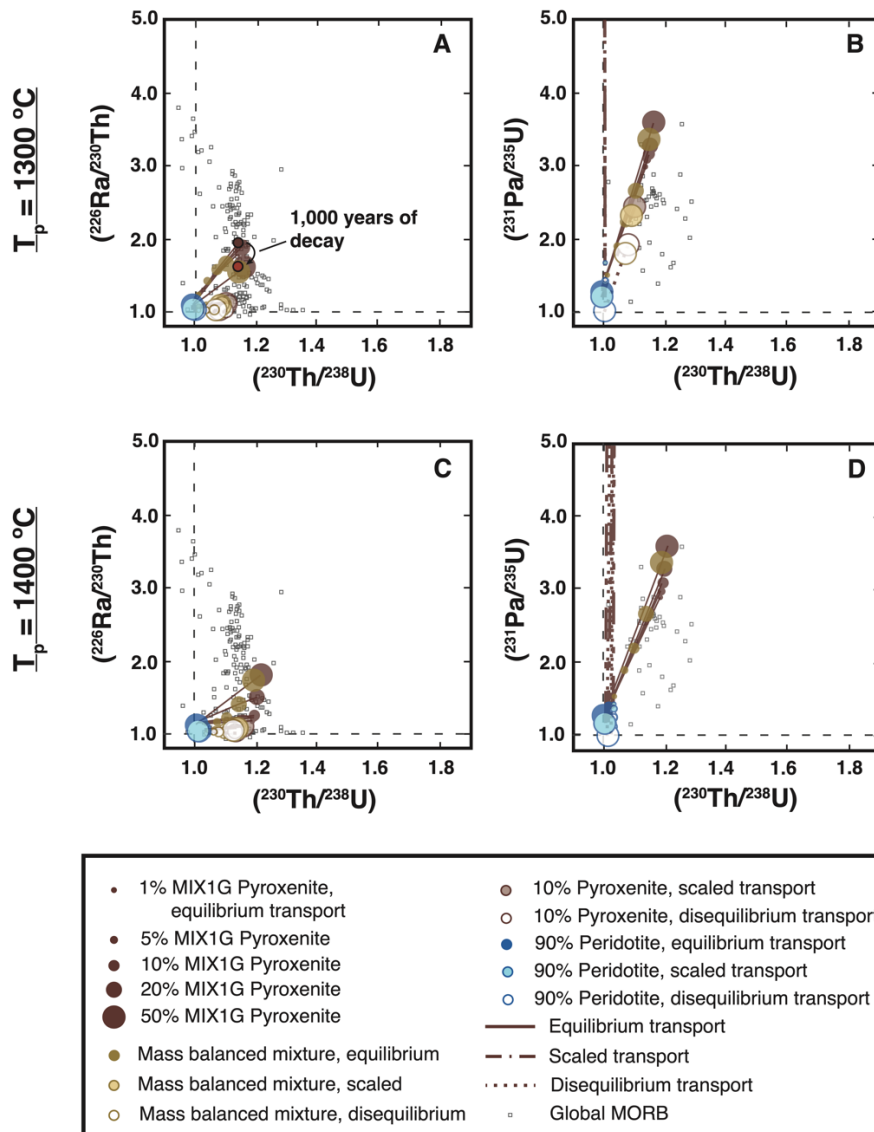


Figure 6. Modeled **A.** $(^{226}\text{Ra}/^{230}\text{Th})$ and **B.** $(^{231}\text{Pa}/^{235}\text{U})$ vs. $(^{230}\text{Th}/^{238}\text{U})$ in partial melt compositions for $T_p = 1300$ 1550 $^\circ\text{C}$, and **C.** $(^{226}\text{Ra}/^{230}\text{Th})$ and **D.** $(^{231}\text{Pa}/^{235}\text{U})$ vs. $(^{230}\text{Th}/^{238}\text{U})$ compositions for $T_p = 1400\text{ }^\circ\text{C}$, for partial melts of MIX1G pyroxenite and coexisting peridotite at a final melting pressure of 5 kbar, as well as mass-balanced binary melt mixtures (see text, Table S1), Calculated results are shown for MIX1G pyroxenite abundances in the solid source of 1 to 50% and a range of magma transport models, all for a representative set of results using a solid mantle upwelling of 3 cm/yr. and a residual maximum porosity of 0.8%. Global MORB data are shown for 1555 comparison, after Figures 1 and 2. The outcome of radioactive decay on $(^{226}\text{Ra}/^{230}\text{Th})$ during 1,024 years of magma transport through the lithosphere is also shown for comparison.

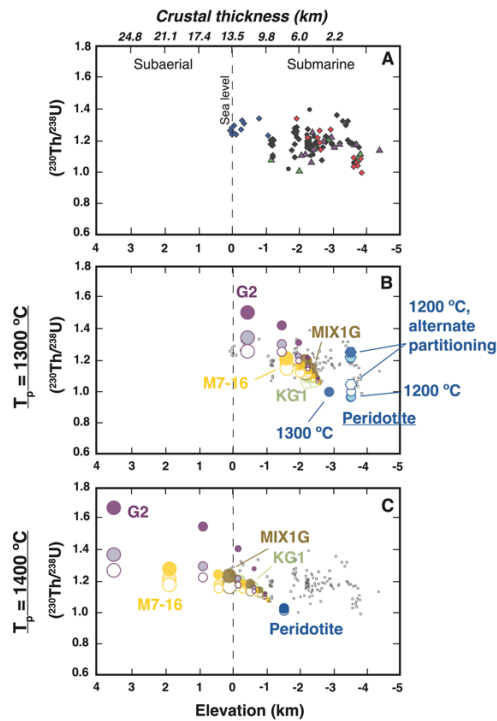


Figure 7. A. Global MORB data after Figure 1, and **B, C.** modeling results for $(^{230}\text{Th}/^{238}\text{U})$ and axial depth after Bourdon et al. (1996), showing partial melt compositions for pure peridotite and peridotite-pyroxenite weighted melt mixtures from this study. Modeling results shown use a solid mantle upwelling rate of 3 cm/yr., a residual maximum porosity of 0.8%, and a mantle potential temperatures of **(B).** 1300 °C and **c.** 1400 °C. Symbols for different peridotite and pyroxenite compositions and magma transport models are similar to those in Figures 3-6, except for simplicity, only mass balanced mixing compositions are shown for pyroxenite scenarios. Additional results for pure peridotite melting at $T_p = 1200\text{ °C}$ are included in panel **(B)** for comparison, with outcomes using alternative U and Th partition coefficients illustrated with hexagon symbols (see text for discussion).

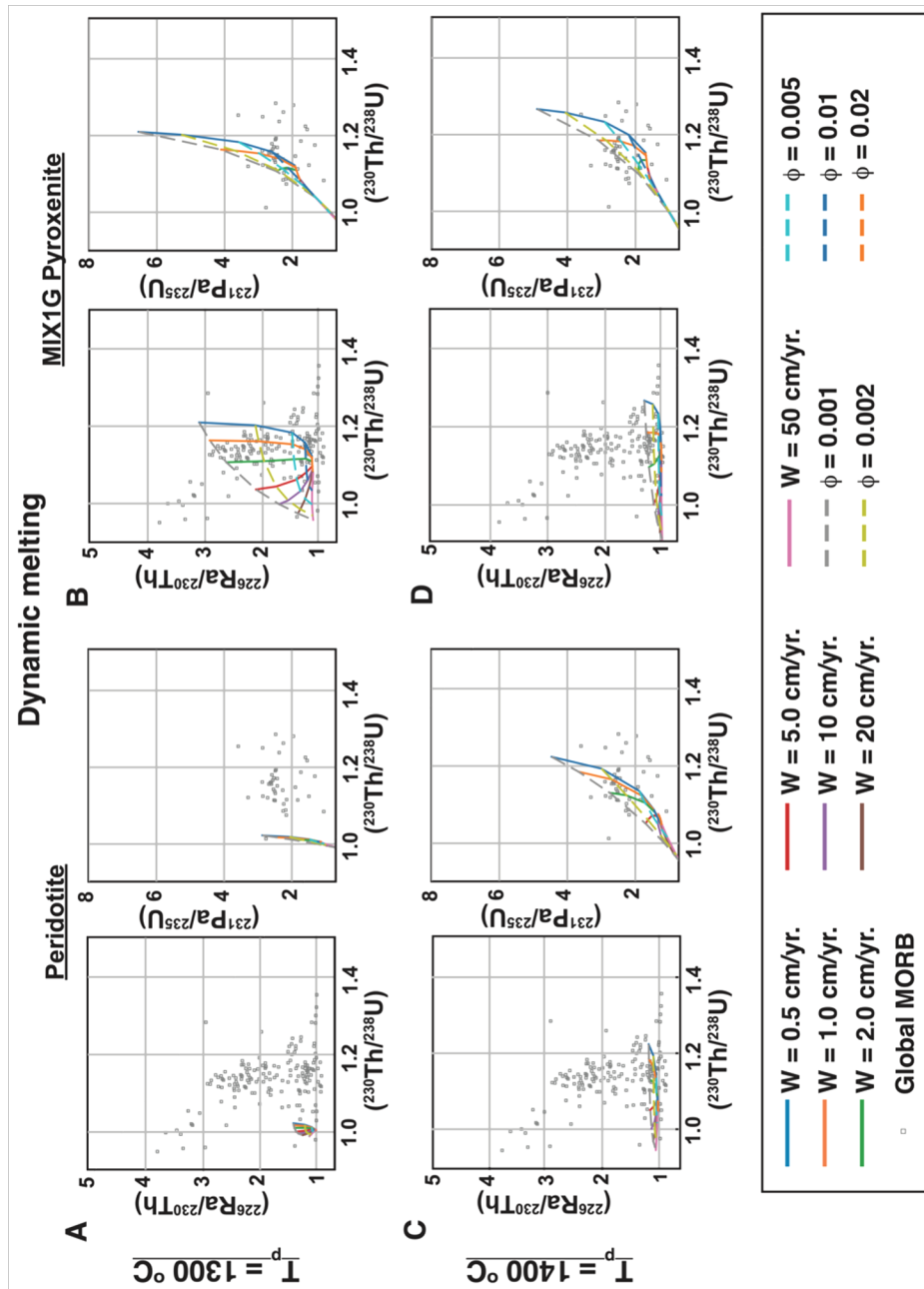


Figure 8. ($^{226}\text{Ra}/^{230}\text{Th}$) and ($^{231}\text{Pa}/^{235}\text{U}$) vs. ($^{230}\text{Th}/^{238}\text{U}$) gridded dynamic melting model results for the solid mantle upwelling rates (W) and residual threshold porosity values (ϕ) listed, with an extracted magma transport rate of 10 m/yr., and showing coexisting **A.** 90% peridotite and **B.** 10% MIX1G pyroxenite partial melt compositions for $T_p = 1300\text{ °C}$, and **C.** 90% peridotite and **D.** 10% MIX1G pyroxenite partial melt compositions for $T_p = 1400\text{ °C}$. Global MORB shown for comparison after Figure 1.

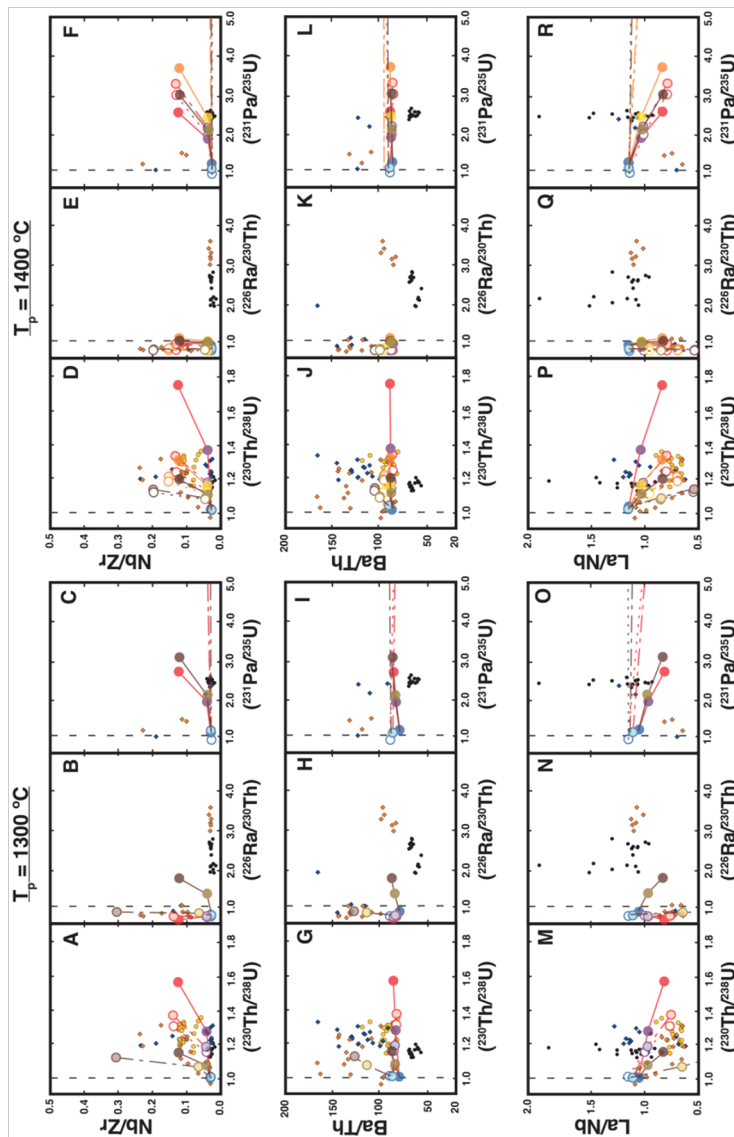


Figure 9. Melt modeling results for (A-F) Nb/Zr, (G-L) Ba/Th, and (M-R) La/Nb, vs. U-series disequilibrium ratios, as labeled and as described in the text. Model compositions are shown for pure peridotite melts (blue), pure pyroxenite melts (G2: red, MIX1G: brown, M7-16: orange), and for pyroxenite-peridotite melt mixtures assuming 10% pyroxenite in the source, with symbols as in Figure 7. Unaltered global MORB data are from Elkins et al. (2011, 2014, 2016a, 2016b), Scott et al. (2018), Sims et al. (2002), and references therein, and have been filtered for age constraints and indicators of chemical alteration using the methods described for Figure 1; symbols are as in Figure 1, except that for simplicity, basalts from all of the far north North Atlantic and Arctic mid-ocean ridges (Mohns, Knipovich, and Gakkel Ridges) are shown using small orange diamonds.

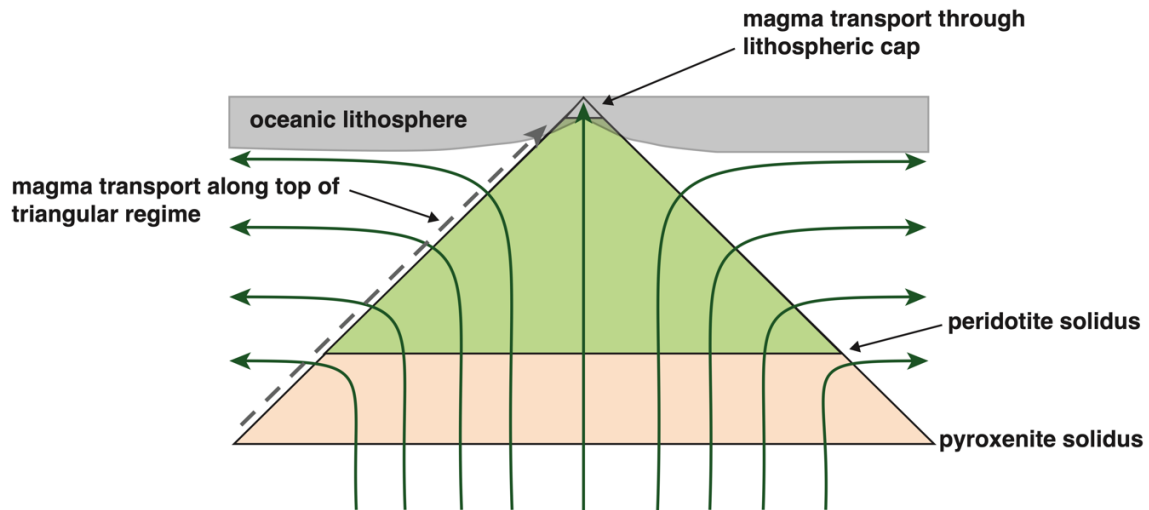
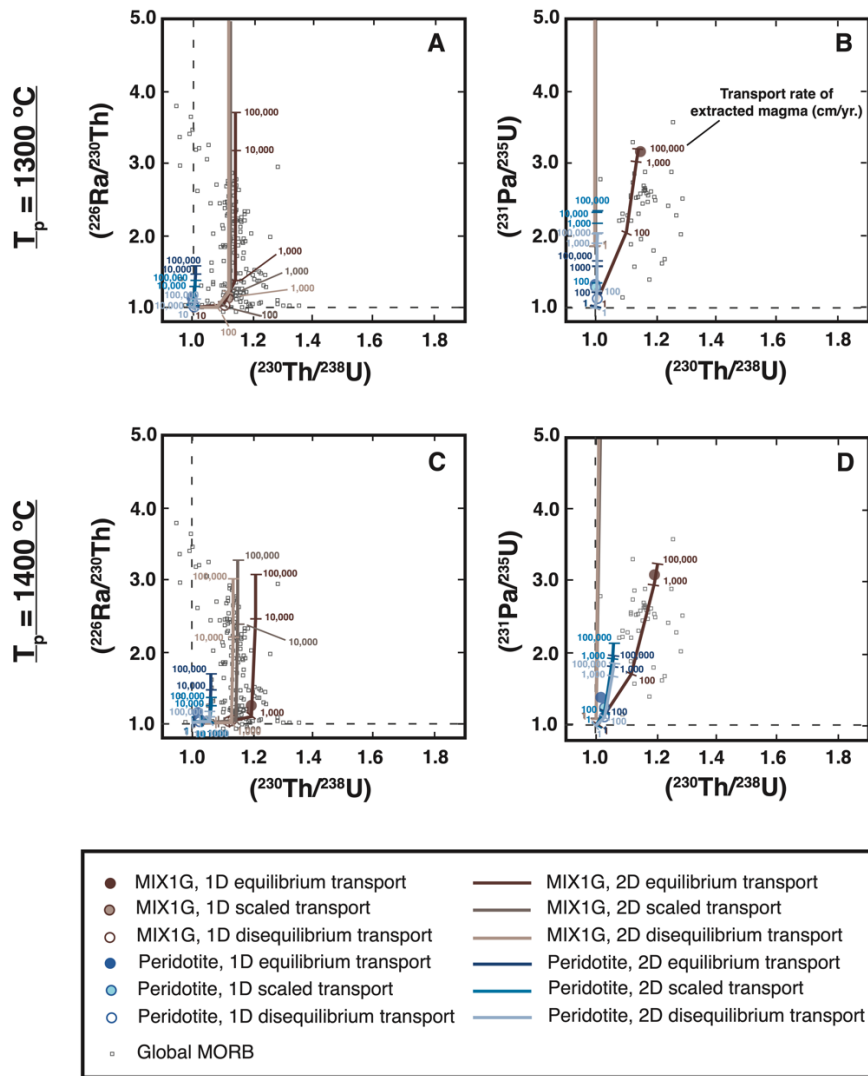


Figure 10. Cartoon illustrating a bilitologic triangular melting regime beneath mid-ocean ridges, after Langmuir et al. (1992) and showing paths along which extracted melts may experience radioactive decay during transport. Melting calculations terminate at final melting pressures of 5 kbar, and experience pure radioactive decay during the final 5 kbar of transport. The integrated two-dimensional melt compositions for the peridotite (green) and pyroxenite (tan) melting regions are then computed for a series of vertical streamlines within the appropriate melting triangle, followed by a radioactive decay interval as magma parcels are transported along the top of the triangular regime and then pool at the central ridge axis.



1590 **Figure 11.** Two-dimensional modeling outcomes for scenarios considering a 10% MIX1G pyroxenite + 90% fertile
 peridotite mantle source with a 3 cm/yr. solid mantle upwelling rate and 0.8% maximum residual porosity, with
 panels after Figure 6. The partial melt compositions shown illustrate the effects of two-dimensional integration (see
 text), with extracted magma transport rates from 1 to 100,000 cm/yr. along the top surface of the triangular melting
 regime (as illustrated in Figure 10). One-dimensional results from Figure 6 are shown for comparison. Magma
 1595 transport rates are labeled for both peridotite (blue) and pyroxenite (brown shades) at appropriate tick locations
 along each melt transport trajectory, and for all three transport models tested. Overall, two-dimensional integration
 with very rapid transport generally enhances isotopic disequilibria, particularly for $(^{226}\text{Ra}/^{230}\text{Th})$ ratios, while very
 slow transport reduces disequilibria due to radioactive decay.

List of Supplementary Materials

1600

Supplementary Tables

Table S1. Summary of melt modeling outcomes for scenarios with solid mantle upwelling rates of 3 cm/yr. and residual maximum porosity of 0.8%.

1605

Table S2. Trace element mineral/melt partition coefficients (D_i) used to calculate bulk rock partition coefficients in model calculations for this study.

Supplementary Data Objects

1610

Data Object S1. This compressed folder is a code directory containing the relevant python code and tools used for this paper, including an updated version of the *pyUserCalc* code (Elkins and Spiegelman 2021), as well as new calculator tools that determine radioactive decay, triangular integration of aggregated partial melts, and dynamic melting outcomes. These files are also available in a public GitLab code repository at <https://gitlab.com/ENKI-portal/pyUsercalc/>.

Data Object S2. This compressed directory contains the tabulated outcomes of *Melt-PX* and *pMELTS* petrologic modeling for this paper, including modes and melt fractions with depth for all model runs.

1615

Data Object S3. This compressed directory includes all of the gridded run results for each melting scenario for this paper, organized into approx. 50 supplementary figures with a series of activity ratio diagrams.